nature structural & molecular biology

Article

https://doi.org/10.1038/s41594-024-01433-0

Substrate translocation and inhibition in human dicarboxylate transporter NaDC3

Received: 19 December 2023

Accepted: 28 October 2024

Published online: 02 December 2024

Check for updates

Yan Li[1], Jinmei Song[1], Vedrana Mikusevic[2], Jennifer J. Marden[1], Alissa Becerril[2,4], Huihui Kuang[3], Bing Wang[3], William J. Rice[1,3], Joseph A. Mindell[2] ✉ & Da-Neng Wang[1] ✉

The human high-affinity sodium–dicarboxylate cotransporter (NaDC3) imports various substrates into the cell as tricarboxylate acid cycle intermediates, lipid biosynthesis precursors and signaling molecules. Understanding the cellular signaling process and developing inhibitors require knowledge of the structural basis of the dicarboxylate specificity and inhibition mechanism of NaDC3. To this end, we determined the cryo-electron microscopy structures of NaDC3 in various dimers, revealing the protomer in three conformations: outward-open C_o, outward-occluded C_{oo} and inward-open C_i. A dicarboxylate is first bound and recognized in C_o and how the substrate interacts with NaDC3 in C_{oo} likely helps to further determine the substrate specificity. A phenylalanine from the scaffold domain interacts with the bound dicarboxylate in the C_{oo} state and modulates the kinetic barrier to the transport domain movement. Structural comparison of an inhibitor-bound structure of NaDC3 to that of the sodium-dependent citrate transporter suggests ways for making an inhibitor that is specific for NaDC3.

The human high-affinity sodium–dicarboxylate cotransporter NaDC3 (SLC13A3) is a member of the human solute carrier 13 family, which also includes the sodium-dependent citrate transporter (NaCT) and a low-affinity dicarboxylate transporter (NaDC1)[1–4]. Expressed in the brain, eye, liver, kidney and placenta[3], NaDC3 imports various dicarboxylates such as succinate, α-ketoglutarate (αKG) and *N*-acetylaspartate (NAA) across the plasma membrane. In the cell, the dicarboxylates function as energy sources, as precursors for the synthesis of lipids and neurotransmitters, as signaling molecules and as osmolytes for cell volume regulation.

While their role at the intersection between the carbon and nitrogen metabolic pathways in the tricarboxylate acid cycle is widely known, it has emerged in recent years that imported dicarboxylates also function as signaling molecules in the cell[5]. αKG binds and regulates a number of enzymes as a master regulator metabolite[6,7]. It extends lifespan in *Caenorhabditis elegans* by inhibiting adenosine triphosphate synthase and target of rapamycin[8], promotes glucose uptake by activating nuclear factor κB signaling[9] and has a major role in cell fate programming by triggering stem cell proliferation[10]. In contrast, succinate and NAA are associated with the inhibition of stem cell differentiation[11,12]. In addition, various dicarboxylate molecules have been found to work in concert to determine cell fate. An elevated αKG-to-succinate ratio promotes histone and DNA demethylation and maintains the pluripotency of embryonic stem cells[13]; in tumor suppressor P53-deficient cells, the higher ratio can drive tumor cell differentiation to antagonize the progression of malignant tumors[14]. Interestingly, manipulating the intracellular αKG-to-succinate ratio by externally applying membrane-permeable αKG derivatives can achieve the same effect[13,14]. Therefore, understanding cell fate determination requires characterizing how NaDC3 selectively imports different substrates and mediates their cytosolic levels[15].

NaDC3 has been found to be involved in a number of disorders[16–19]. Among them, the most lethal may be Canavan disease (CD), an early-onset central nervous system disorder characterized by 'spongiform'

[1]Department of Cell Biology, New York University School of Medicine, New York, NY, USA. [2]Porter Neuroscience Research Center, National Institute of Neurological Disorders and Stroke, National Institutes of Health, Bethesda, MD, USA. [3]Cryo-Electron Microscopy Core, New York University School of Medicine, New York, NY, USA. [4]Present address: Department of Medicine, University of California, San Francisco, San Francisco, CA, USA. ✉e-mail: mindellj@ninds.nih.gov; da-neng.wang@med.nyu.edu

https://doi.org/10.1038/s41594-024-01433-0

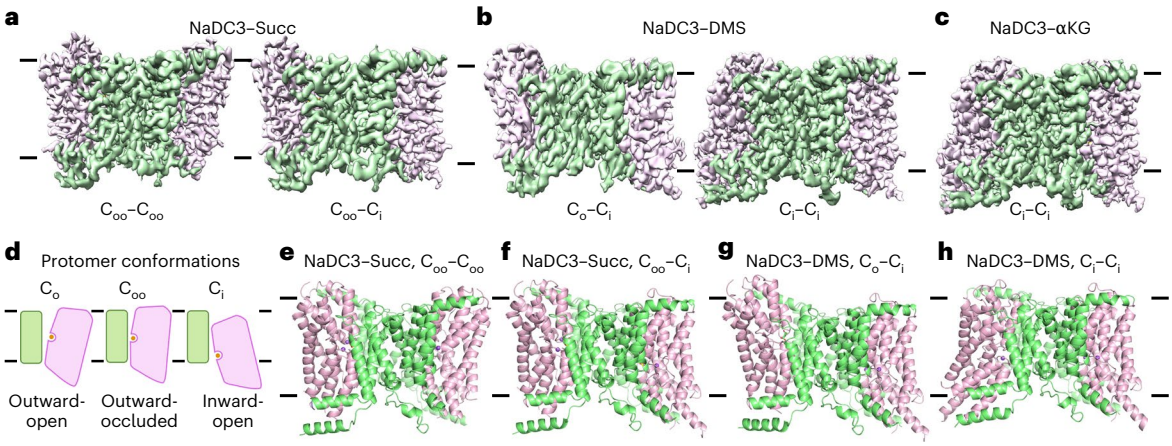

Fig. 1 | Cryo-EM structures of NaDC3. a, NaDC3 purified in the presence of succinate yielded two cryo-EM maps, a 2.53-Å map of an outward-occluded, symmetric C_{oo}–C_{oo} dimer and a 2.60-Å map of an outward-occluded, inward-open, asymmetric C_{oo}–C_i dimer. **b**, NaDC3 in DMS also gave two maps, a 2.92-Å map of an outward-open, inward-open, asymmetric C_o–C_i dimer and a 2.17-Å map of an inward-open, symmetric C_i–C_i dimer. **c**, NaDC3 in αKG gave a 2.09-Å map of an inward-open symmetric, C_i–C_i dimer. **d**, Schematic drawings of the three conformations of an NaDC3 protomer: outward-open C_o, outward-facing occluded C_{oo} and inward-open C_i. **e**–**h**, Structural models of NaDC3 in various substrates: NaDC3–succinate, C_{oo}–C_{oo} dimer (**e**); NaDC3–succinate, C_{oo}–C_i dimer (**f**); NaDC3–DMS, C_o–C_i dimer (**g**); NaDC3–DMS, C_i–C_i dimer (**h**). The maps and models are viewed from within the membrane plane, whereas the scaffold and transport domains are colored light green and light pink, respectively.

vacuolation of white matter, caused by excessive accumulation of NAA[20]. In the brain, NAA is imported by NaDC3 into oligodendrocytes and its overload in the brains of persons with CD arises from loss-of-function mutations in a gene encoding an enzyme responsible for breaking down NAA[20–23]. The accumulation of NAA in glial cells leads to neurotoxicity and causes 'osmotic stress', resulting in the loss of the myelin sheath and vacuolation of the brain[24–27].

Inhibition of the dicarboxylate transporter has been suggested as a possible treatment for persons with CD[27,28]. Disruption of NAA import into glial cells by *SLC13A3* gene knockdown is effective in preventing leukodystrophy in CD mice[28]. Lithium, an inhibitor of NaDC3, can lower NAA levels in the brains of both healthy and CD rodents[29,30] and has shown positive results in human clinical studies[31–33]. Though small-molecule NaDC3 inhibitors have also been identified[34], more potent and specific inhibitors of NaDC3 are desired, particularly over the neuronally expressed NaCT.

No NaDC3 structure has yet been determined; moreover, the molecular mechanism of the transporter and the nutrient uptake process are poorly defined. In this work, using single-particle cryo-electron microscopy (cryo-EM) and biochemical assays, we aimed to establish the structural basis of the anionic substrate specificity of NaDC3, to elucidate its conformational changes from outward facing to inward facing and to understand the mechanisms of its inhibition.

Results

Various conformations with different dicarboxylates

NaDC3 cotransports Na^+ and dicarboxylate in a 3:1 ratio[22,35]. Using both whole-cell transport assays and a two-electrode voltage clamp, we validated that NaDC3 is active (Extended Data Fig. 1a,b). We overexpressed and purified the wild-type (WT) human NaDC3 protein (Extended Data Fig. 1c,d). The presence of Li^+, a cation that inhibits the transporter[35,36], helped to stabilize the protein samples that yielded interpretable cryo-EM maps (Fig. 1a–c). The dissociation constant (K_d) for succinate in NaDC3 is 17.6 ± 9.8 μM; that for another substrate, 2,3-dimethylsuccinate (DMS), is 10.2 ± 5.6 μM (Fig. 2a). These measurements agree with the Michaelis–Menten constant (K_m) of 15–20 μM previously determined in whole cells[2,35,37]. The affinity of NaDC3 to substrate αKG is lower (Fig. 2a)[38].

As an importer, the interaction of NaDC3 with a substrate occurs in three stages: recognizing and distinguishing the substrate upon binding from the extracellular space, translocating the substrate across the membrane and releasing the substrate molecule to the cytosol. Thus, to understand the structural basis of NaDC3's substrate specificity and translocation requires structural information of the transporter in at least three conformations: outward-open, occluded and inward-open (Fig. 1d).

To this end, we used single-particle cryo-EM to determine structures of NaDC3 in the presence of each of the three substrates[35,38]: succinate, DMS and αKG (Fig. 1, Table 1 and Extended Data Figs. 1–6 and 7a). All the maps reveal a dimer structure. Like other divalent anion–sodium symporter (DASS) transporters[39,40], each protomer in NaDC3 comprises a scaffold domain and a transport domain (Extended Data Fig. 8a). The transport domains in the dimers, carrying a bound substrate, are located at various heights in the membrane, corresponding to different conformations of NaDC3 in the elevator mechanism (Fig. 1)[41,42]. However, because of the presence of Li^+, the sodium positions were not always well defined. We, thus, focused on the interaction of the transporter with the substrate.

NaDC3 purified in 100 mM NaCl and 20 mM succinate yielded two maps, a symmetric dimer at 2.53-Å resolution and an asymmetric dimer at 2.60-Å resolution (Fig. 1a, Table 1 and Extended Data Figs. 1f, 2a, 3a,b and 5a). The symmetric dimer adopts a conformation with the substrates bound to both protomers near the outer side of the transporter but without an aqueous pathway to the external solution on either side. Both protomers are, therefore, in outward-occluded conformations; we denote this state as C_{oo}–C_{oo} (Figs. 1e and 2d and Extended Data Fig. 5b). In contrast, while one protomer in the asymmetric dimer is in a similar outward-occluded C_{oo} conformation, the other is in a substrate-bound, inward-open conformation, which we refer to as C_i. This dimer is, thus, in the C_{oo}–C_i state (Figs. 1f and 2e and Extended Data Fig. 5c).

NaDC3 purified in DMS also yielded two cryo-EM maps, an asymmetric dimer at 2.92-Å resolution and a symmetric dimer at 2.17-Å resolution (Fig. 1b, Table 1 and Extended Data Figs. 1g, 2b, 3c,d and 5a). One protomer in this asymmetric dimer is in the C_i state observed above, whereas the other protomer is outward facing. Unlike the C_{oo}–C_i dimer in succinate, in which the outward-facing protomer is in an occluded conformation, this protomer is open to the external solution, an 'outward-open' state that we designate C_o. Thus, the protomers in the asymmetric NaDC3 C_o–C_i dimer in DMS are both 'open' with clear

https://doi.org/10.1038/s41594-024-01433-0

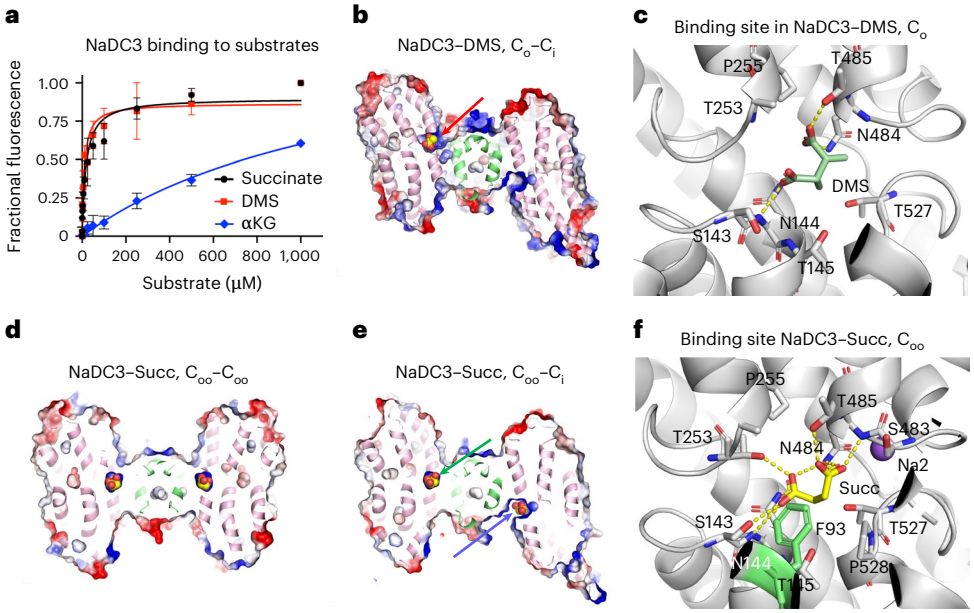

Fig. 2 | Dicarboxylate-binding sites in NaDC3 in the outward-open and outward-occluded conformations. a, NaDC3 binding to succinate ($n = 3$), DMS ($n = 4$) and αKG ($n = 3$), as measured by intrinsic tryptophan fluorescence in solution. The fluorescence changes for αKG did not reach saturation even at a substrate concentration of 2.5 mM; thus, the calculation of K_d was not possible; n refers to the number of individual binding experiments that were each performed in triplicate and the error bars indicate the s.d. **b**, Cross-section of NaDC3–DMS, C_o–C_i dimer, shown as electrostatic surface together with the secondary structures in the scaffold (light green) and transport (light pink) domains. The dicarboxylate-binding sites in the C_o and C_i protomers are open to the extramembraneous space. The red arrow indicates the substrate entry pathway and the direction of the view in **c**. **c**, Substrate-binding site in the C_o protomer of NaDC3–DMS. All the residues involved in substrate binding are from within the transport domain. Dashed lines indicate polar interactions. **d**, Cross-section of NaDC3–succinate, C_{oo}–C_{oo} dimer. **e**, Cross-section of NaDC3–succinate, C_{oo}–C_i dimer. The dicarboxylate-binding site in the outward-occluded C_{oo} protomers in **d**,**e** are closed to the extracellular space. The green arrow represents the direction of the view in **f**, while the blue arrow indicates the substrate exit pathway. **f**, Dicarboxylate-binding site in the C_{oo} protomer of NaDC3–succinate. In addition to all the residues involved in substrate binding being from the transport domain, F93 (green) from the scaffold domain makes a van der Waals contact with the bound succinate. The interaction observed in the C_{oo} state is more extensive than that in the C_o state.

paths to the extracellular or intracellular space (Figs. 1g and 2b and Extended Data Fig. 5d). In this map, a substrate is visualized only in the C_o state. In the second DMS map, the symmetric dimer reveals both protomers in the C_i–C_i state (Figs. 1h and 3a and Extended Data Fig. 5e). Similarly, in αKG, a 2.09-Å cryo-EM map of NaDC3 shows the protein as an inward-open, symmetric C_i–C_i dimer, with both protomers bound to substrate molecules (Figs. 1c and 3d, Table 1 and Extended Data Figs. 1h, 2c, 3e and 5a,f). Lastly, purification in the low-affinity substrate NAA did not yield stable samples; thus, structure determination in that substrate was not attempted.

In addition to the conservation in domain organization, in all these NaDC3 structures, no matter what conformation, the transmembrane topology is conserved (Extended Data Fig. 5g) and parallel to the structure of NaCT, another SLC13 family member[43].

Dicarboxylate binding, recognition and differentiation

Therefore, we observed a collection of NaDC3 conformations, including C_o (outward-open), C_{oo} (outward-occluded) and C_i (inward-open). This wide range of states, including several with different bound dicarboxylates, yields insight into the nature of substrate binding, translocation and release.

In the outward-open C_o state (from the NaDC3–DMS protomer), the dicarboxylate site is exposed to the extracellular space (Fig. 2b). A DMS density is found in the cavity (Extended Data Figs. 6a and 7a), which is coordinated by polar interaction of residues entirely in the transport domain, including N144 (both side chain and backbone) to one DMS carboxylate moiety and with N484 and T485 to the other (Fig. 2c). These residues are part of the two SNT motifs from the tips of hairpins HP_{in} and HP_{out}, respectively (Extended Data Fig. 5g), which are conserved across the broad DASS family[39,40].

In the next conformation, outward-occluded C_{oo}, visualized in three of the four succinate-bound protomers, the substrate-binding site is closed to both sides of the membrane (Fig. 2d,e). This observation, combined with the height of the transport domain, led us to name the conformation as the outward-occluded state, C_{oo}. Density for a succinate molecule is found in the binding pocket, coordinated by elements of the two SNT motifs, as well as a TxP motif (T253-x254-P255 from loop L5ab) in the N-terminal half of the domain and a TP motif (T527-P528 from loop L10ab) from the C-terminal half (Fig. 2f and Extended Data Figs. 5g and 6b). Specifically, the two carboxylate moieties of succinate are coordinated by polar interaction with the side chains of S143 and T253 on one end and the backbone oxygen of N484 and the side chain of T485 on the other. Such interactions in the C_{oo} pocket are notably more extensive than those observed for DMS in the C_o state (Fig. 2c). The substrate interaction with the TxP and TP motifs was not previously observed in inward-open C_i structures of homologous proteins[39,43–45] but the critical role of these motifs is consistent with published mutagenesis studies of NaDC3 (ref. 15). In another novel observation, the bound succinate also interacts with a residue contributed by the scaffold domain, making a van der Waals interaction with F93, a residue that is located 4.0 Å away (Fig. 2f and Extended Data Figs. 4b and 6b). This phenylalanine residue is conserved among Na^+-dependent transporters of the DASS family. Overall, the substrate-binding pocket has an electropositive surface, suitable for accommodating the negatively charged succinate (Extended Data Fig. 7b).

Comparison of the substrate-binding site in C_o and C_{oo} shows that the pocket becomes more compact in the occluded state (Extended Data Fig. 8d). Within each of two 'vertical' pairs of residues, P255–T145 and T485–P528, the distances decreased from 10.3 Å and 10.5 Å to 9.4 Å and 9.7 Å, respectively, in the occluded state.

https://doi.org/10.1038/s41594-024-01433-0

Table 1 | Cryo-EM data collection, refinement and validation statistics for NaDC3

	NaDC3–succinate, C_{oo}–C_{oo} (EMD-42621), (PDB 8UVI)	NaDC3–succinate, C_{oo}–C_i (EMD-42617), (PDB 8UVE)	NaDC3–DMS, C_o–C_i (EMD-42619), (PDB 8UVG)	NaDC3–DMS, C_i–C_i (EMD-42618), (PDB 8UVF)	NaDC3–αKG, C_i–C_i (EMD-42615), (PDB 8UVC)	NaDC3–PF4a, C_i–C_i (EMD-42616), (PDB 8UVD)
Data collection						
Magnification	105,000	105,000	105,000	105,000	105,000	105,000
Voltage (kV)	300	300	300	300	300	300
Electron exposure (e^- per Å^2)	52.58	52.58	52.58, 51.58, 48.8	52.58, 51.58, 48.8	53.11	57.25, 48.8
Defocus range (μm)	−0.9 to −1.9	−0.9 to −1.9	−0.9 to −1.9	−0.9 to −1.9	−0.8 to −1.4	−0.8 to −1.4
Pixel size (Å)	0.4125	0.4125	0.4125	0.4125	0.4125	0.4125
Symmetry imposed	*C2*	*C1*	*C1*	*C2*	*C2*	*C2*
Initial particle images (no.)	2,932,803	2,932,803	6,894,596	6,894,596	1,567,382	2,917,656
Final particle images (no.)	202,740	228,347	60,488	397,856	330,891	476,543
Map resolution (Å)	2.53	2.60	2.92	2.17	2.09	2.16
FSC threshold	0.143	0.143	0.143	0.143	0.143	0.143
Map resolution range (Å)	2.2–3.4	1.8–3.7	2.4–5.6	1.9–2.8	1.9–2.7	1.95–3.0
Refinement						
Initial model used (AlphaFold code)	Q8WWT9	Q8WWT9	Q8WWT9	Q8WWT9	Q8WWT9	Q8WWT9
Model resolution (Å)	2.7	2.9	3.2	2.4	2.3	2.4
FSC threshold	0.5	0.5	0.5	0.5	0.5	0.5
Model resolution range (Å)	N/A	N/A	N/A	N/A	N/A	N/A
Map sharpening *B* factor (Å^2)	−87	−89.2	−96.9	−70.3	−61	−49.9
Model composition						
Nonhydrogen atoms	8,212	8,406	8,353	8,520	8,558	8,622
Protein residues	994	1,010	1,010	1,026	1,026	1,026
Ligands	Succinate: 2	Succinate: 2	DMS: 1	N/A	αKG: 2	PF4a: 2
Ions	Na^+: 2	Na^+: 2	Na^+: 2	Na^+: 4	Na^+: 2	Na^+:4
B factors (Å^2)						
Protein	44.60	87.61	76.17	39.25	42.60	49.45
Ligand	49.59	94.36	84.99	52.82	54.36	63.82
R.m.s.d.						
Bond lengths (Å)	0.003	0.003	0.003	0.003	0.003	0.002
Bond angles (°)	0.595	0.650	0.696	0.591	0.664	0.577
Validation						
MolProbity score	1.51	1.49	1.48	1.45	1.47	1.41
Clashscore	9.69	8.36	9.01	7.76	7.34	7.76
Poor rotamers (%)	0.60	0.00	0.12	0.47	0.53	0.23
Ramachandran plot						
Favored (%)	98.78	98.50	98.10	99.41	99.41	98.62
Allowed (%)	1.22	1.5	1.90	0.59	0.59	1.38
Disallowed (%)	0.00	0.00	0.00	0.00	0.00	0.00

FSC, Fourier shell correlation; N/A, not applicable.

https://doi.org/10.1038/s41594-024-01433-0

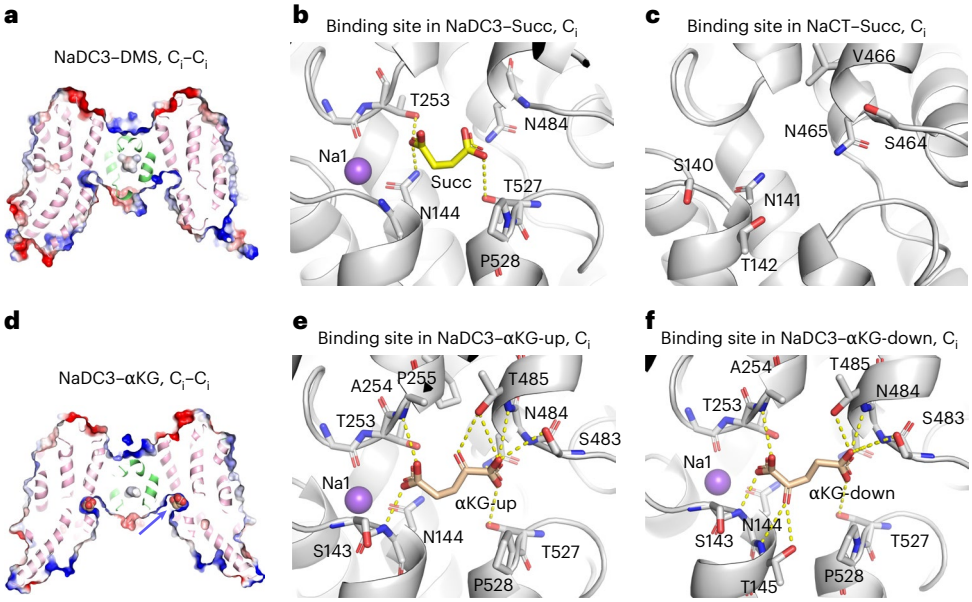

Fig. 3 | Dicarboxylate-binding sites in NaDC3 and NaCT in the inward-open conformation. a, Cross-section of NaDC3–DMS, C_i–C_i dimer, shown as an electrostatic surface together with secondary structures. The dicarboxylate-binding sites in both C_i protomers are open to the cytosol. **b**, Dicarboxylate-binding site in the C_i protomer of NaDC3–succinate. All the residues involved in substrate binding are from the transport domain. The structure is viewed in the direction as indicated by the blue arrow in Fig. 2e. **c**, Dicarboxylate-binding site in the C_i protomer of the homologous NaCT protein determined in the presence of succinate, C_i–C_i dimer. The overall structure of the protein is similar to that previously determined in the presence of citrate[43]. No dicarboxylate density was found at the binding site. **d**, Cross-section of NaDC3–αKG, C_i–C_i dimer. The dicarboxylate-binding sites in both C_i protomers are open to the cytosol. The blue arrow indicates the substrate exit pathway and the direction of the view in **e**,**f**. **e**,**f**, Dicarboxylate-binding site in the C_i protomer of NaDC3–αKG, C_i–C_i dimer. In each protomer, αKG is found to bind in two opposite directions, with its hydroxyl group pointing either to the extracellular space (**e**; up) or to the cytosol (**f**; down). All the residues involved in dicarboxylate binding are from within the transport domain.

These substrate-bound C_o and C_{oo} structures suggest that substrate recognition and differentiation by NaDC3 occur in two stages. The initial binding stage is achieved through the interaction of the two SNT motifs with the two carboxylate moieties in the C_o conformation. This step is responsible for substrate recognition. Following the initial binding, the transporter converts to an outward-facing, occluded C_{oo} conformation, in which the substrate is totally enclosed in a compact pocket, where the TxP and TP motifs, in addition to the two SNTs, participate in substrate binding.

Such a hypothesis on the structural basis of substrate specificity is in agreement with the previously published modeling-based mutagenesis results[46]. Substituting any residue in the first SNT motif (S143-N144-T145) reduced succinate transport activity in NaDC3 (ref. 15). Likewise, substitutions in the second SNT motif (S483-N484-T485) in human NaDC3 or the equivalent residues in rabbit NaDC1 had similar deleterious effects[15,47]. In particular, substitution of the asparagine in either SNT motif completely abolished substrate transport. These results support the central role of the two SNT motifs in the recognition of the substrate in the C_o and C_{oo} states (Fig. 2c,f). Furthermore, substituting the TxP (T253-x254-P255) and, in particular, the TP (T527-P528) motifs in both human NaDC3 and NaDC1 was found to greatly change their transport activity[15,48], consistent with the direct interaction of the two motifs with the substrate observed in the occluded C_{oo} state (Fig. 2f). Lastly, the A254N substitution occurring at the x position in the TxP motif causes acute reversible leukoencephalopathy[18]. The introduction of the negatively charged aspartate residue to the pocket likely affects the binding of the dicarboxylate anion (Extended Data Fig. 7d,e), abolishing αKG uptake and resulting in its accumulation in the urine.

Interestingly, all the residues in the binding pocket are conserved among human NaDC3, NaCT and NaDC1, except the x in the TxP motif and T485 in the second SNT motif (Extended Data Fig. 7c). The x is an alanine in NaDC3 and either a threonine or glycine in SLC13 proteins from other species. The threonine in the C-terminal SNT motif is replaced by a valine in NaCT and NaDC1; perhaps these subtle changes account for the variations in specificity seen among subtypes and homologs in the SLC13 family[4]. Consistent with such a model, substitution of T485 to an alanine (found in rabbit NaDC1) or methionine (found in a human NaDC1 variant)[49] resulted in transporters with specific changes in affinity for citrate[15].

Structural basis of dicarboxylate release

In the third major protomer conformation, C_i, we observe the transport domain in NaDC3–succinate to shift substantially toward the inner face of the membrane, as expected for an elevator-type transporter (Fig. 1). This translocation moves the substrate-binding site to a position exposed to the cytoplasmic aqueous medium (Fig. 3a). The succinate in this state is now coordinated by polar interaction, through the side chains of N144, T253 and T527 (Fig. 3b and Extended Data Fig. 6c). In addition, the succinate only makes van der Waals contacts with N484 and P528. As in the case of the outward-open conformation, all the binding site residues reside within the transport domain. Notably, in this state, the F93 residue from the scaffold domain is located 6.1 Å away from the bound succinate. Compared to the compact substrate-binding site in the occluded C_{oo} state, the substrate site in the open C_i state is more 'relaxed' along the membrane normal (Extended Data Fig. 8e); the distances between P255 and T145 and between T485 and P528 are increased from 9.8 Å to 11.6 Å and from 9.8 Å to 11.8 Å, respectively. We regard this structure as the substrate prerelease state in the inward-open conformation.

To better understand the process of substrate release, we determined the structure of NaDC3 in the presence of αKG, a medium-affinity substrate for the transporter (Figs. 1c and 3d–f and Extended Data Figs. 5a,f and 6d). The 2.09-Å cryo-EM structure of NaDC3–αKG shows the transporter as an inward-open C_i–C_i dimer, with a density found at the substrate site. The density represents a mixture of αKG molecules bound to the transporter in two different orientations, with the

https://doi.org/10.1038/s41594-024-01433-0

Table 2 | Cryo-EM data collection, refinement and validation statistics for NaCT

	NaCT–succinate, C_i–C_i (EMD-42620) (PDB 8UVH)	NaCT–PF4a, C_i–C_i (EMD-42614) (PDB 8UVB)
Data collection		
Magnification	105,000	105,000
Voltage (kV)	300	300
Electron exposure (e^- per Å^2)	52.75	61.19
Defocus range (μm)	−0.8 to −1.9	−0.8 to −1.9
Pixel size (Å)	0.4125	0.4125
Symmetry imposed	*C2*	*C2*
Initial particle images (no.)	3,125,207	6,132,038
Final particle images (no.)	323,571	745,845
Map resolution (Å)	2.33	2.13
FSC threshold	0.143	0.143
Map resolution range (Å)	2.1–2.7	1.9–2.4
Refinement		
Initial model used (PDB code)	7JSK	7JSK
Model resolution (Å)	2.7	2.4
FSC threshold	0.5	0.5
Model resolution range (Å)	N/A	N/A
Map sharpening *B* factor (Å^2)	−90.5	−74.6
Model composition		
Nonhydrogen atoms	7,158	7,204
Protein residues	918	918
Ligands	N/A	PF4a: 2
Ions	N/A	Na^+: 4
B factors (Å^2)		
Protein	52.62	49.30
Ligand	44.55	40.00
R.m.s.d.		
Bond lengths (Å)	0.003	0.004
Bond angles (°)	0.602	0.662
Validation		
MolProbity score	1.48	1.60
Clashscore	8.60	9.59
Poor rotamers (%)	0.26	0.51
Ramachandran plot		
Favored (%)	99.11	98.88
Allowed (%)	0.89	1.12
Disallowed (%)	0.00	0.00

carbonyl group pointing either to the extracellular space (up) or the cytosol (down) (Fig. 3e,f and Extended Data Fig. 6d). The differences between the densities for the two αKG orientations were too small to be separated during classification by the image processing procedure. While, in both αKG orientations, the carboxylate moieties interact with the same residues, S143 and T253 at one end and S483, T485 and T527 at the other, the carbonyl group of αKG in the up pose interacts with the side chain of T485 while, in the down pose, it interacts with the backbone oxygen of N144 and the side chain of T145 (Fig. 3e,f).

Moreover, the C_i protomers of NaDC3 in the C_o–C_i or C_i–C_i dimer determined in the presence of DMS did not show a substrate density (Fig. 3a). We suspect that this low occupancy is a result of reduced affinity of the substrate to the transporter in the inward-open C_i state. Because DMS density is visible in the outward-open C_o state (Extended Data Fig. 6a), these observations suggest that the importer's affinity to DMS is asymmetric on the two sides of the membrane: with higher affinity in the C_o state for substrate binding and lower affinity in the C_i state to favor substrate release.

To characterize how the homologous neuronal transporter NaCT differs from NaDC3 in their substrate release, we also determined the structure of human NaCT in the presence of succinate in a C_i–C_i conformation at 2.33-Å resolution (Fig. 3c, Table 2 and Extended Data Figs. 1j, 2e, 3g and 5a). The structure is similar to that previously determined in the presence of another substrate, citrate[43]. Whereas the side chain densities at the substrate-binding site are well resolved, the succinate density is again invisible, likely a result of the low affinity of NaCT to succinate[4]. Comparison of the substrate site between NaDC3 and NaCT (Fig. 3b,c) shows that the binding site residues are conserved at the same locations. At the second SNT motif, however, the threonine residue is replaced by a valine in NaCT, for which the side chain cannot form a polar interaction with the succinate.

Conformational changes between the C_o and C_i states

Available data from homologous proteins suggest that NaDC3 translocates substrates between the C_o and C_i conformations through an elevator-type movement of the transport domain in each protomer[40]. The simultaneous visualization of the WT NaDC3 in outward-open, outward-occluded and inward-open conformations provides us with an opportunity to quantitatively analyze the conformational changes and to more rigorously examine the rigid-body movement assumption[39,50].

The cryo-EM structures of NaDC3 determined in three different substrates yielded five different dimers (Fig. 1 and Extended Data Fig. 5) and their substrate-bound protomers can be classified into three conformations: C_o, C_{oo} and C_i. These observations immediately suggest that the outward-open to inward-open transition for substrate import occurs in at least two steps: C_o to C_{oo} first followed by C_{oo} to C_i. The NaDC3 scaffold domain forms a framework, which includes three horizontal helices H4c, H6b and H9c on the membrane surface linking to the transport domain through the loops, L4-HP_{in}, L6-6b and L9-HP_{out} (Fig. 4a,b and Extended Data Fig. 8a). Within the scaffold domain framework, the transport domain moves from the C_o to C_{oo} conformation by a 5.9-Å vertical translation and a 14° tilt (as measured for a straight line connecting S241 and I230 in TM5a) relative to the membrane and a 10° rotation within the membrane plane (Fig. 4c,f and Supplementary Videos 1 and 2). This is followed by a transition from the occluded to inward-open conformation, realized by the transport domain's further 11.9-Å translation, 27° tilt and 14° rotation (Fig. 4d,f). In total, the transport domain undergoes a 17.8-Å translation, 41° tilt and 24° rotation from the outward-open to the inward-open conformations to translocate the bound substrate across the membrane (Fig. 4g).

We next examined the structural invariance of the scaffold domain and the degree that the transport domain adheres to the rigid-body assumption. The scaffold domain in our five substrate-bound NaDC3 structures stays rigid for the C_o, C_{oo} and C_i conformations, with a root-mean-square deviation (r.m.s.d.) of 0.407–0.519 Å for the backbone α-carbons (Fig. 4a and Extended Data Fig. 8b). Only the horizontal helices H6b and H9c tilt or bend slightly between conformations, while the transmembrane helices remain structurally invariant. Furthermore, the dimer interface between the scaffold domains is also structurally invariant, with an r.m.s.d. of 0.277–0.732 Å among the four types of dimer structures (Extended Data Fig. 8c), consistent with previous evidence of independent operation of the protomers in other DASS proteins[50]. Lastly, the transport domain for the C_o, C_{oo} and C_i conformations has an r.m.s.d. ranging from 0.535 to 0.694 Å (Extended Data Fig. 8f), indicating a rigid-body movement with only minor structural changes (Fig. 4b). In agreement with this observation, the transport

https://doi.org/10.1038/s41594-024-01433-0

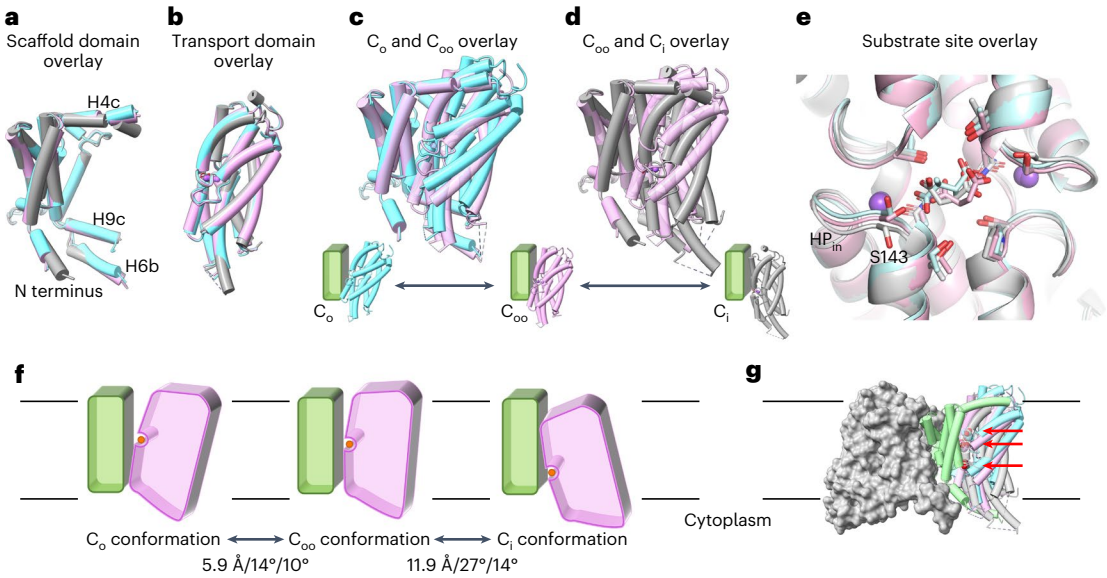

Fig. 4 | Conformational transition of NaDC3 through C_o, C_{oo} and C_i conformations. a, Structural overlay of the scaffold domains of NaDC3 for the C_o (light blue, in NaDC3–DMS C_o–C_i dimer), C_{oo} (light pink, in NaDC3–succinate C_{oo}–C_{oo} dimer) and C_i (light gray, in NaDC3–succinate C_{oo}–C_i dimer) conformations, viewed from within the membrane plane. The scaffold domain is invariant. **b**, Overlay of the transport domains for the C_o, C_{oo} and C_i conformations after alignment. The structure of the transport domain is largely invariant, with minor changes at the substrate-binding site. **c**, Overlay of the NaDC3 protomers between the C_o and C_{oo} conformations. The transition from the C_o to C_{oo} conformation is realized by a 5.9-Å translation, 14° tilt and 10° rotation. **d**, Overlay of the NaDC3 protomers between the C_{oo} and C_i conformations. The transition from the C_{oo} to C_i conformation is realized by an 11.9-Å translation, 27° tilt and 14° rotation. In **c**,**d**, the transport domains in the three conformations are shown as inserts. **e**, Overlay of the dicarboxylate-binding sites for the C_o, C_{oo} and C_i conformations. The substrate-binding site is largely conserved but the tip of the HP_{in} hairpin loop moves away from the substrate in the C_o and C_i conformations, resulting in an ~1-Å opening of the dicarboxylate-binding site. In addition, the direction of the S143 side chain varies in the three NaDC3 conformations. **f**, Schematic drawing showing the rigid-body movement of the transport domain relative to the scaffold domain during substrate import. The orange sphere represents the bound substrate along with the cotransported sodium ions. **g**, Movement of the bound substrate along with the transport domain across the membrane. The left protomer is shown in surface presentation C_{oo}. In the protomer on the right, the scaffold domain in C_{oo} (light green) is shown together with an overlay of transport domain in C_o (light blue), C_{oo} (light pink) and C_i (light gray). The movement of the substrate (shown in spheres) from the outward-open to inward-open conformation is indicated by red arrows.

domain in the NaDC3 dimers displays higher *B* factors than the scaffold domains (Extended Data Fig. 8g).

The simultaneous observation of C_o and C_i state structures of WT NaDC3 also allowed us to further examine another aspect of the rigid-body movement assumption (namely, symmetry of the substrate-binding site between the two sides of the membrane). While both being more relaxed compared to the occluded state, the substrate sites in the C_o state and the C_i state are somewhat asymmetrical, especially on the N-terminal half. The backbones of the L5ab loop and the tip of HP_{in} are ~1 Å more separated along the membrane normal in the C_i conformation than in the C_o state (Fig. 4e) and the side chain of S143 from the first SNT motif points in opposite directions between the two conformations.

It is unclear how the relative movement of the transport domain to the scaffold domain is regulated or how the movement is supported at the domain interface. Across the C_o, C_{oo} and C_i conformations, the side chain of the scaffold domain residue F93 that directly interacts with the bound substrate in the occluded C_{oo} conformation switches between an upward and a downward direction in the C_{oo} occluded and C_o or C_i open conformations (Fig. 5a,b and Extended Data Fig. 4) raises the possibility that this residue modulates the kinetic barrier traversed by the transport domain during translocation. This orientation change of the F93 side chain may alter the interaction between the transport and scaffold domains. In agreement with a critical role of F93, we found that its substitution to a smaller residue, either an alanine or a valine, completely abolished NaDC3's transport activity (Fig. 5c). However, when substituted to the bulkier tyrosine, the transporter showed reduced activity, despite similar trafficking to the plasma membrane (Extended Data Fig. 9a,b). This F93Y mutant showed a 40% reduction in maximum rate of succinate uptake (V_{max}) with little change in K_m (Fig. 5d and Extended Data Fig. 9c,d), supporting the proposed role for F93 in affecting translocation kinetics.

Inhibition mechanisms

As inhibition of NaDC3 transport offers a promising therapy to reduce NAA accumulation in the glial cells of persons suffering from Canavan disease[26,27], we characterized the inhibition mechanism of NaDC3. A desired inhibitor will not only need to have high affinity but also have to be specific to NaDC3 over other proteins, particularly the homologous neuronal citrate transporter NaCT.

Several types of NaDC3 inhibitors have been developed and identified. PF4a (PF-06761281, (*R*)-hydroxy-methoxy-methylpyridinyl-ethyl-succinate) inhibits both NaDC3 and NaCT[34]. The compound is both a substrate and an inhibitor of the two transporters, implying that it can enter the cell and, most likely, inhibit from the cytosolic side of the membrane[51]. PF4a inhibits the transport activity of human NaDC3 in HEK293 cells at a half-maximal inhibitory concentration (IC_{50}) of 39.2 μM (Fig. 6a). We solved the cryo-EM structure of the transporter protein bound to PF4a (Fig. 6b–d, Table 1 and Extended Data Figs. 1i, 2d, 3f, 5a and 10a,b). The NaDC3–PF4a structure is at 2.16-Å resolution and the protein dimer is in a symmetric inward-open C_i–C_i conformation.

PF4a binds to the substrate site in the C_i conformation, with its carboxylate moieties interacting with the two SNT motifs (Fig. 6e,f). Surprisingly, at the binding site for the pyridine ring of PF4a we observed two densities, separated by a ~110° rotation, in which the pyridine ring can fit (Extended Data Fig. 10a). There are two possible interpretations: either the ring in PF4a rotates and interacts with NaDC3 in two

https://doi.org/10.1038/s41594-024-01433-0

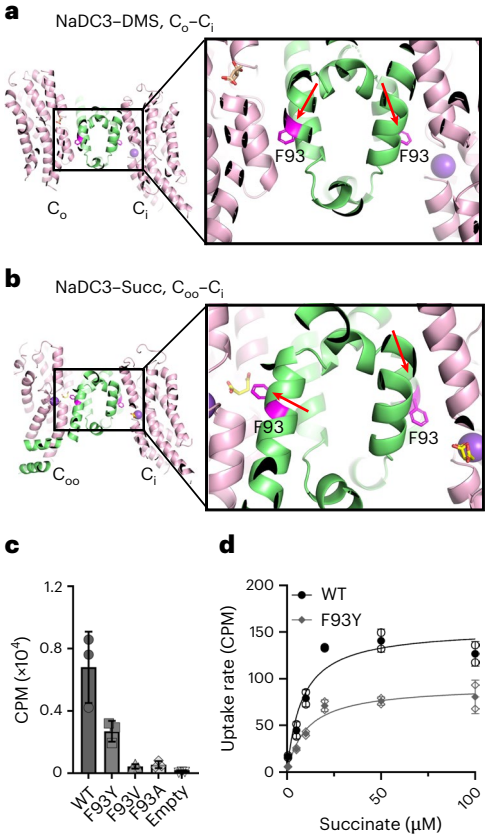

Fig. 5 | Role of residue F93 at the domain interface in regulating the movement of the transport domain. a, Central section of the NaDC3–DMS, C_o–C_i dimer structure. In the C_o and C_i protomers, the side chain of F93 of the scaffold domain points downward and is >6.5 Å away from the substrate site. **b**, Central section of the NaDC3–succinate, C_{oo}–C_i dimer structure. In the C_{oo} protomer, the side chain of F93 is tilted upward, making a van der Waals contact with the bound substrate (at 4 Å). In **a**,**b**, the arrows indicate the directions of the F93 side chain in various NaDC3 conformations. **c**, Radioactive succinate uptake into HEK293 cells expressing WT NaDC3 or one of three different F93 mutants. Bars represent the mean values obtained from three experiments, each conducted with 15 μM total succinate and 15 nM [^{3}H]succinate ($n = 3$). Error bars depict the s.d. The phenylalanine substitution to a valine or alanine completely abolished the transport activity (F93V versus WT, $P = 0.0086$; F93A versus WT, $P = 0.0093$), indicating the critical role of the residue. The substitution to a tyrosine, however, retained ~30% of the activity (F93Y versus WT, $P = 0.0406$), suggesting that a bulky side chain is required at this location for the transporter to function. All P values were obtained from unpaired two-sided t-tests. **d**, Kinetics of succinate uptake in HEK293 cells by EGFP–NaDC3 WT and F93Y mutant ($n = 4$). Solid symbols represent the average initial succinate uptake rates from two independent experiments across varying concentrations. The WT NaDC3 and F93Y mutant exhibit comparable Michaelis–Menten constants with K_m values of 8.0 ± 5.1 μM and 10.5 ± 5.9 μM, respectively. The V_{max} for the WT is 154.3 ± 26.3 CPM and that for the F93Y mutant is 92.6 ± 15.0 CPM. The open symbols represent the results of the individual biological replicates. The error bars on solid symbols depict the s.d. from four data points (two technical replicates from each of the two biological replicates).

orientations or the compound purchased from Sigma (PZ0318) is a mixture of the (*R*) and (*S*) forms (PF4a and PF4b). To rule out the second possibility, we measured the one-dimensional ^{1}H nuclear magnetic resonance (NMR) spectra of the compound (Extended Data Fig. 10b). The chemical shifts observed in DMSO-d_6 agree with those published for PF4a (ref. 34). This confirmed that the commercial compound is indeed the pure (*R*) form. Thus, PF4a binds to NaDC3 as two rotamers, rotamer 1 and rotamer 2 (Fig. 6e,f). The internal flexibility of PF4a allows the molecule to bind to NaDC3 in either conformation, depending on the structure of the binding site.

Both rotamers occupy the substrate site. The carboxylate moieties of PF4a rotamer 1 form polar interactions with N144 (backbone), T145 (both backbone and side chain), T253, T527 and Na^+ (Fig. 6e). In addition to the above interactions, rotamer 2 forms a polar interaction with T145 (Fig. 6f). These interactions mimic those of the substrate with the binding site (Fig. 3). There are also additional van der Waals contacts for the pyridine ring. The ring in rotamer 1 interacts with F93, L97, P426 and I429 on the cytosolic surface of the scaffold domain (Fig. 6h). Rotamer 2 makes contact with L59, I429 and L432, with its pyridine ring inserting between the scaffold and transport domains like a wedge (Fig. 6i). We propose that such interactions with the PF4a pyridine ring prevent the movement of the transport domain between the C_i and C_o states required for substrate translocation, thus locking the transporter in its C_i conformation.

Comparison of PF4a binding to NaDC3 and NaCT, the two dicarboxylate and tricarboxylate transporters in the brain, may suggest ways to modify the inhibitor to make it more specific to NaDC3. To this end, we determined the cryo-EM structure of NaCT bound to PF4a to 2.13-Å resolution (Fig. 6g, Table 2 and Extended Data Figs. 1k, 2f and 3h). The transporter is in its C_i–C_i conformation and its overall structure resembles that of NaCT previously determined in the presence of another inhibitor, PF2 (ref. 43). However, PF4a binds to NaCT in only one orientation (Fig. 6g and Extended Data Fig. 10c), in a similar manner to rotamer 1 in NaDC3 (Fig. 6e). The inhibitor molecule in NaCT is coordinated by polar interactions with N141 (both backbone and side chain), T142 (both backbone and side chain), T227, G228 (backbone), V466 (backbone), N465 (both backbone and side chain) and T508 (Fig. 6g). The ring of PF4a inhibits the domain movement by interacting with the cytosolic surface of the transport scaffold domain, making contacts with F90, P407 and I410 of the scaffold domain. This inhibition mechanism resembles that of PF2 (ref. 43) but the angles of the aromatic ring differ between the two cases.

Discussion

In this work, we determined the cryo-EM structures of WT NaDC3 in C_o–C_i, C_{oo}–C_{oo}, C_{oo}–C_i and C_i–C_i conformations (Fig. 1 and Extended Data Fig. 5). Because NaDC3 works as an importer under physiological conditions, we reason that the outward-open C_o conformation and its transition to the C_{oo} state, instead of the prerelease C_i state, are where dicarboxylate binding and recognition occur (Fig. 2b). The two SNT signature motifs conserved in the DASS protein family[39,44] are chiefly responsible for binding and recognition of dicarboxylates (Fig. 2c). Next, the transporter changes to the occluded C_{oo} state, in which the substrate is enclosed tightly within the binding pocket (Fig. 2d,e). As the dicarboxylate site is largely composed of amino acids from the tips of hairpins HP_{in} and HP_{out}, and of intrahelix loops L5ab and L10ab, both polar side chains and backbone α-carbons in these loop regions can directly form polar interactions with the substrate. Importantly, in addition to the two SNT motifs and the two TxP and TP motifs from the loops in the transport domain, F93 from the scaffold domain also comes into contact with the dicarboxylate in this occluded state (Fig. 2f). The availability of the C_o and C_{oo} structures with various dicarboxylate substrates bound may now facilitate a computational evaluation of the energy landscape of the transition between these states, providing further insight into the structural basis of NaDC3's substrate specificity. Lastly, in the prerelease C_i state of NaDC3, the dicarboxylate is coordinated loosely and can interact with the binding site in multiple ways (Fig. 3) raising the possibility that this represents a low-affinity state, facilitating substrate release. Establishing the structural basis of its substrate specificity will allow us to further understand how NaDC3 regulates the fate of both healthy and tumor cells.

Simultaneous observation of NaDC3 structures in the C_o, C_{oo} and C_i states shows the extent of its structural dynamics. The scaffold domain in the protomer is invariant, whereas the transport domain of NaDC3 switches among the C_o, C_{oo} and C_i states largely as a rigid body,

https://doi.org/10.1038/s41594-024-01433-0

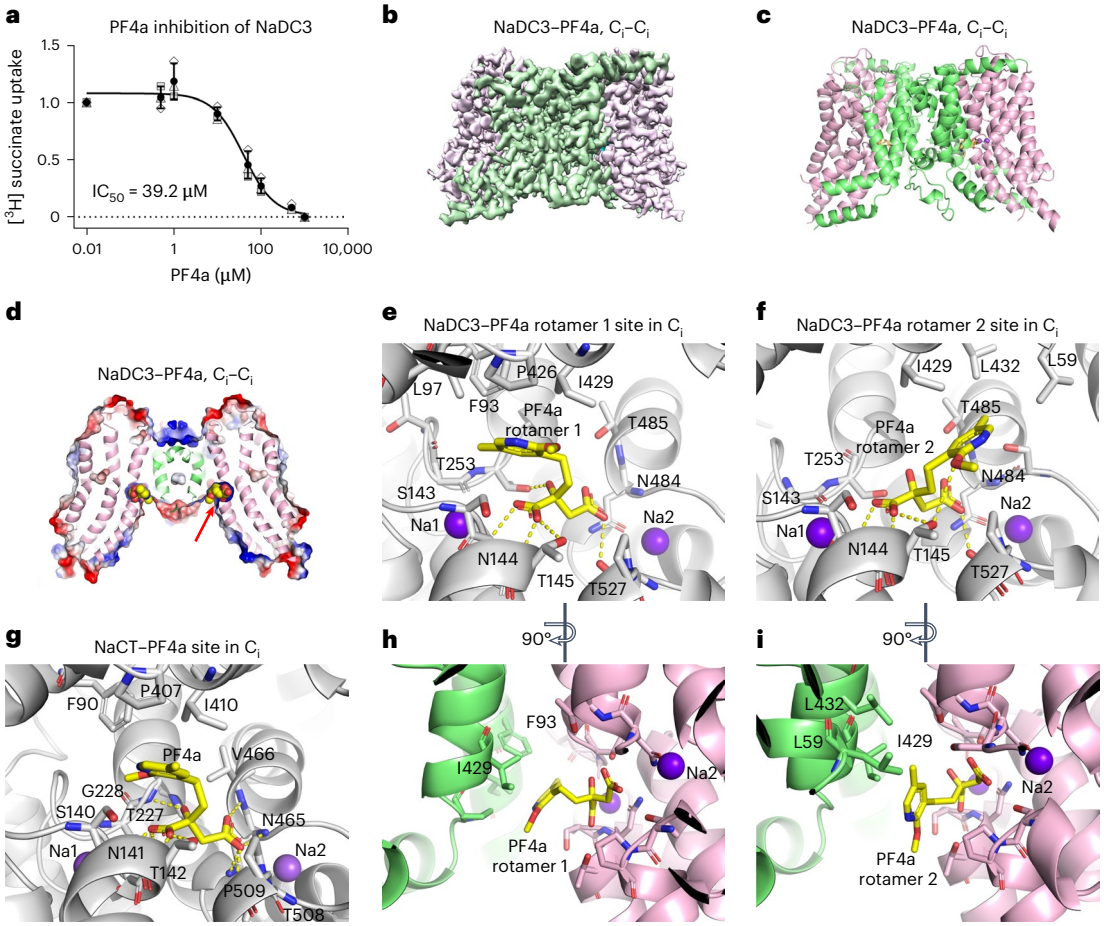

Fig. 6 | Inhibitor-binding sites in human NaDC3 and NaCT. a, Succinate transport activity in HEK293 cells expressing NaDC3 in the presence of the inhibitor PF4a. Normalized data were fit with a single-site dose–response curve with an IC_{50} of 39.2 µM. Results of individual experiments are shown as squares, diamonds and triangles, with each shape representing an average of three biological replicates. Dark symbols are the means of three independent experiments. Error bars depict the s.d. **b**, A 2.16-Å map of NaDC3 determined in the presence of inhibitor PF4a, showing a symmetric C_i–C_i dimer. **c**, Structural model of NaDC3–PF4a. **d**, Cross-section of the NaDC3–PF4a structure. **e**,**f**, In each protomer, PF4a is found to bind in two different ways, as rotamer 1 (**e**) and rotamer 2 (**f**). While the dicarboxylate moieties of the two rotamers bind to the same position at the substrate site, the pyridine rings of the inhibitor bind in different orientations. **g**, Inhibitor-binding site in the homologous NaCT protein, determined in the presence of PF4a. The overall structure of the protein is similar to that previously determined in the presence of another inhibitor, PF2 (ref. 43). PF4a binds to NaCT in a similar way to rotamer 1 in NaDC3. **h**, Rotamer 1 binding site in NaDC3 viewed from within the membrane. **i**, Rotamer 2 binding site in NaDC3 viewed from within the membrane.

with some minor structural changes at the substrate site (Fig. 4a–e). Comparison of our structures also reveals the degree of motion that the transport domain needs to undergo the C_o-to-C_i transition and the structural framework that supports this motion (Fig. 4a–d,f and Supplementary Videos 1 and 2). Here, we observed two steps comprising this transition, from outward-open to outward-occluded and then to inward-open. For both steps, transmembrane and horizontal helices in the scaffold domain provide a framework for the movement of the transport domain.

While rigid-body movement of the transport domain is confirmed, it is unclear whether the conformational changes are modulated by other interactions between the scaffold and transport domains. With F93, we observed an aromatic residue at the scaffold and transport domain interface that changes its orientation among the C_o, C_{oo} and C_i conformations (Fig. 5a,b), making contact with the bound substrate only in the occluded state. Together with kinetic measurements (Fig. 5d and Extended Data Fig. 9), this suggests a role for F93 in the energetics of the transition. In addition, it will be intriguing to see whether the rotation of this phenylalanine residue is coupled to substrate binding.

NaDC3 forms a dimer, raising the possibility of cooperative transport between the protomers. Our observations that NaDC3 can adopt C_{oo}–C_{oo} and C_i–C_i symmetric dimers and C_o–C_i and C_{oo}–C_i asymmetric dimers under the same conditions suggest that the two protomers do not work cooperatively or anticooperatively[52,53]. This is in agreement with a recent study on the conformational dynamics of the bacterial homolog VcINDY, in which single-molecule fluorescence resonance energy transfer measurements suggested an asymmetrical C_o–C_i dimer[52].

The inhibitor PF4a adopts two rotamers when bound to NaDC3, with rotamer 2 inserting between the scaffold and transport domains as a wedge. This wedge likely acts to reduce the movement of the transport domain required for substrate translocation. The observation that, in the homologous NaCT protein, PF4a binds in only one orientation (Fig. 6g), similar to that of rotamer 1 (Fig. 6e), suggests that, if the inhibitor can be modified in such a way that it adopts a structure similar to rotamer 2 (Fig. 6f), it may yield an NaDC3-specific inhibitor. Lastly, in addition to small molecules binding to the transporter from the cytosolic side, the availability of structures in the C_o and C_{oo} conformations now allows for the design of conformation-specific inhibitors from the extracellular side. It is possible that some nonsubstrates can bind to such states, generating a high energy barrier for state transition and preventing substrate transport. Such molecules might also be candidates for pharmacological inhibitors.

Online content

Any methods, additional references, Nature Portfolio reporting summaries, source data, extended data, supplementary information, acknowledgements, peer review information; details of author contributions and competing interests; and statements of data and code availability are available at https://doi.org/10.1038/s41594-024-01433-0.

References

1. Markovich, D. & Murer, H. The SLC13 gene family of sodium sulphate/carboxylate cotransporters. *Pflugers Arch.* **447**, 594–602 (2004).
2. Pajor, A. M. Molecular properties of the SLC13 family of dicarboxylate and sulfate transporters. *Pflugers Arch.* **451**, 597–605 (2006).
3. Bergeron, M. J., Clemencon, B., Hediger, M. A. & Markovich, D. SLC13 family of Na^+-coupled di- and tri-carboxylate/sulfate transporters. *Mol. Asp. Med.* **34**, 299–312 (2013).
4. Pajor, A. M. Sodium-coupled dicarboxylate and citrate transporters from the SLC13 family. *Pflugers Arch.* **466**, 119–130 (2014).
5. Baker, S. A. & Rutter, J. Metabolites as signalling molecules. *Nat. Rev. Mol. Cell Biol.* **24**, 355–374 (2023).
6. Huergo, L. F. & Dixon, R. The emergence of 2-oxoglutarate as a master regulator metabolite. *Microbiol. Mol. Biol. Rev.* **79**, 419–435 (2015).
7. Di Conza, G., Tsai, C. H. & Ho, P. C. Fifty shades of α-ketoglutarate on cellular programming. *Mol. Cell* **76**, 1–3 (2019).
8. Chin, R. M. et al. The metabolite α-ketoglutarate extends lifespan by inhibiting ATP synthase and TOR. *Nature* **510**, 397–401 (2014).
9. Wang, X. et al. α-Ketoglutarate-activated NF-κB signaling promotes compensatory glucose uptake and brain tumor development. *Mol. Cell* **76**, 148–162 (2019).
10. Song, J. et al. α-Ketoglutarate promotes pancreatic progenitor-like cell proliferation. *Int. J. Mol. Sci.* **19**, 943 (2018).
11. Weber, A. et al. Succinate accumulation is associated with a shift of mitochondrial respiratory control and HIF-1α upregulation in PTEN negative prostate cancer cells. *Int. J. Mol. Sci.* **19**, 2129 (2018).
12. Long, P. M. et al. *N*-Acetylaspartate (NAA) and *N*-acetylaspartylglutamate (NAAG) promote growth and inhibit differentiation of glioma stem-like cells. *J. Biol. Chem.* **288**, 26188–26200 (2013).
13. Carey, B. W., Finley, L. W., Cross, J. R., Allis, C. D. & Thompson, C. B. Intracellular α-ketoglutarate maintains the pluripotency of embryonic stem cells. *Nature* **518**, 413–416 (2015).
14. Morris, J. P. T. et al. α-Ketoglutarate links p53 to cell fate during tumour suppression. *Nature* **573**, 595–599 (2019).
15. Schlessinger, A., Sun, N. N., Colas, C. & Pajor, A. M. Determinants of substrate and cation transport in the human Na^+/dicarboxylate cotransporter NaDC3. *J. Biol. Chem.* **289**, 16998–17008 (2014).
16. Zhunussova, A. et al. Tumor microenvironment promotes dicarboxylic acid carrier-mediated transport of succinate to fuel prostate cancer mitochondria. *Am. J. Cancer Res* **5**, 1665–1679 (2015).
17. Stellmer, F. et al. 3-Hydroxyglutaric acid is transported via the sodium-dependent dicarboxylate transporter NaDC3. *J. Mol. Med.* **85**, 763–770 (2007).
18. Dewulf, J. P. et al. *SLC13A3* variants cause acute reversible leukoencephalopathy and α-ketoglutarate accumulation. *Ann. Neurol.* **85**, 385–395 (2019).
19. Wong, K. N. et al. Novel *SLC13A3* variants and cases of acute reversible leukoencephalopathy and α-ketoglutarate accumulation and literature review. *Neurol. Genet* **9**, e200101 (2023).
20. Moffett, J. R., Ross, B., Arun, P., Madhavarao, C. N. & Namboodiri, A. M. *N*-Acetylaspartate in the CNS: from neurodiagnostics to neurobiology. *Prog. Neurobiol.* **81**, 89–131 (2007).
21. Matalon, R. & Michals-Matalon, K. Biochemistry and molecular biology of Canavan disease. *Neurochem. Res.* **24**, 507–513 (1999).
22. Huang, W. et al. Transport of *N*-acetylaspartate by the Na^+-dependent high-affinity dicarboxylate transporter NaDC3 and its relevance to the expression of the transporter in the brain. *J. Pharmacol. Exp. Ther.* **295**, 392–403 (2000).
23. Morland, C. & Nordengen, K. *N*-Acetyl-aspartyl-glutamate in brain health and disease. *Int. J. Mol. Sci.* **23**, 1268 (2022).
24. Maier, H., Wang-Eckhardt, L., Hartmann, D., Gieselmann, V. & Eckhardt, M. *N*-Acetylaspartate synthase deficiency corrects the Myelin phenotype in a Canavan disease mouse model but does not affect survival time. *J. Neurosci.* **35**, 14501–14516 (2015).
25. Baslow, M. H. & Guilfoyle, D. N. Canavan disease, a rare early-onset human spongiform leukodystrophy: insights into its genesis and possible clinical interventions. *Biochimie* **95**, 946–956 (2013).
26. Pleasure, D. et al. Pathophysiology and treatment of Canavan disease. *Neurochem. Res.* **45**, 561–565 (2020).
27. Wei, H. et al. The pathogenesis of, and pharmacological treatment for, Canavan disease. *Drug Discov. Today* **27**, 2467–2483 (2022).
28. Wang, Y. et al. Ablating the transporter sodium-dependent dicarboxylate transporter 3 prevents leukodystrophy in Canavan disease mice. *Ann. Neurol.* **90**, 845–850 (2021).
29. O'Donnell, T. et al. Chronic lithium and sodium valproate both decrease the concentration of *myo*-inositol and increase the concentration of inositol monophosphates in rat brain. *Brain Res.* **880**, 84–91 (2000).
30. Baslow, M. H., Kitada, K., Suckow, R. F., Hungund, B. L. & Serikawa, T. The effects of lithium chloride and other substances on levels of brain *N*-acetyl-L-aspartic acid in Canavan disease-like rats. *Neurochem. Res.* **27**, 403–406 (2002).
31. Janson, C. G. et al. Lithium citrate for Canavan disease. *Pediatr. Neurol.* **33**, 235–243 (2005).
32. Assadi, M. et al. Lithium citrate reduces excessive intra-cerebral *N*-acetyl aspartate in Canavan disease. *Eur. J. Paediatr. Neurol.* **14**, 354–359 (2010).
33. Solsona, M. D., Fernandez, L. L., Boquet, E. M. & Andres, J. L. Lithium citrate as treatment of Canavan disease. *Clin. Neuropharmacol.* **35**, 150–151 (2012).
34. Huard, K. et al. Optimization of a dicarboxylic series for in vivo inhibition of citrate transport by the solute carrier 13 (SLC13) family. *J. Med. Chem.* **59**, 1165–1175 (2016).
35. Wang, H. et al. Structure, function, and genomic organization of human Na^+-dependent high-affinity dicarboxylate transporter. *Am. J. Physiol. Cell Physiol.* **278**, C1019–C1030 (2000).
36. Chen, X., Tsukaguchi, H., Chen, X. Z., Berger, U. V. & Hediger, M. A. Molecular and functional analysis of SDCT2, a novel rat sodium-dependent dicarboxylate transporter. *J. Clin. Invest.* **103**, 1159–1168 (1999).
37. Pajor, A. M. Molecular cloning and functional expression of a sodium–dicarboxylate cotransporter from human kidney. *Am. J. Physiol.* **270**, F642–F648 (1996).
38. Burckhardt, B. C., Lorenz, J., Kobbe, C. & Burckhardt, G. Substrate specificity of the human renal sodium dicarboxylate cotransporter, hNaDC-3, under voltage-clamp conditions. *Am. J. Physiol. Renal Physiol.* **288**, F792–F799 (2005).
39. Mancusso, R., Gregorio, G. G., Liu, Q. & Wang, D. N. Structure and mechanism of a bacterial sodium-dependent dicarboxylate transporter. *Nature* **491**, 622–626 (2012).
40. Sauer, D. B. et al. The ups and downs of elevator-type di-/tricarboxylate membrane transporters. *FEBS J.* **289**, 1515–1523 (2022).

41. Drew, D. & Boudker, O. Shared molecular mechanisms of membrane transporters. *Annu. Rev. Biochem.* **85**, 543–572 (2016).
42. Garaeva, A. A. & Slotboom, D. J. Elevator-type mechanisms of membrane transport. *Biochem. Soc. Trans.* **48**, 1227–1241 (2020).
43. Sauer, D. B. et al. Structure and inhibition mechanism of the human citrate transporter NaCT. *Nature* **591**, 157–161 (2021).
44. Nie, R., Stark, S., Symersky, J., Kaplan, R. S. & Lu, M. Structure and function of the divalent anion/Na^+ symporter from *Vibrio cholerae* and a humanized variant. *Nat. Commun.* **8**, 15009 (2017).
45. Sauer, D. B. et al. Structural basis of ion–substrate coupling in the Na^+-dependent dicarboxylate transporter VcINDY. *Nat. Commun.* **13**, 2644 (2022).
46. Schlessinger, A., Khuri, N., Giacomini, K. M. & Sali, A. Molecular modeling and ligand docking for solute carrier (SLC) transporters. *Curr. Top. Med. Chem.* **13**, 843–856 (2013).
47. Pajor, A. M. Conformationally sensitive residues in transmembrane domain 9 of the Na^+/dicarboxylate co-transporter. *J. Biol. Chem.* **276**, 29961–29968 (2001).
48. Colas, C., Pajor, A. M. & Schlessinger, A. Structure-based identification of inhibitors for the SLC13 family of Na^+/dicarboxylate cotransporters. *Biochemistry* **54**, 4900–4908 (2015).
49. Pajor, A. M. & Sun, N. N. Single nucleotide polymorphisms in the human Na^+–dicarboxylate cotransporter affect transport activity and protein expression. *Am. J. Physiol. Renal Physiol.* **299**, F704–F711 (2010).
50. Mulligan, C. et al. The bacterial dicarboxylate transporter VcINDY uses a two-domain elevator-type mechanism. *Nat. Struct. Mol. Biol.* **23**, 256–263 (2016).
51. Huard, K. et al. Discovery and characterization of novel inhibitors of the sodium-coupled citrate transporter (NaCT or SLC13A5). *Sci. Rep.* **5**, 17391 (2015).
52. Kinz-Thompson, C. D. et al. Elevator mechanism dynamics in a sodium-coupled dicarboxylate transporter. Preprint at *bioRxiv* https://doi.org/10.1101/2022.05.01.490196 (2022).
53. Holzhüter, K. & Geertsma, E. R. Functional (un)cooperativity in elevator transport proteins. *Biochem. Soc. Trans.* **48**, 1047–1055 (2020).

Methods

Overexpression and purification of NaDC3

Baculovirus bearing the codon-optimized human *SLC13A3* gene (obtained from the RESOLUTE Consortium[54], Addgene, 161475) with an N-terminal 10xHis–TEV tag was prepared using the Bac-to-Bac system and amplified in the *Spodoptera frugiperda* Sf9 cell line (Expression Systems, 94-001S). Protein was produced in *Trichoplusia ni* BTI-Tn-5B1-4 cell line (Expression Systems, 94-002S) at 27 °C for 72 h. Cells were harvested and lysed in a buffer of 50 mM Tris pH 8.0, 400 mM NaCl, 20 mM lithium succinate and 10% glycerol. Membranes were isolated by ultracentrifugation and solubilized in a buffer of 50 mM Tris pH 8.0, 200 mM NaCl, 20 mM lithium succinate, 10% glycerol and 1% glyco-diosgenin (GDN; Anatrace). NaDC3 was purified on a Ni^{2+}-NTA affinity column and subsequently a Superdex 200 10/300 GL size-exclusion column equilibrated in buffer (25 mM Tris pH 7.5, 100 mM NaCl, 0.02% GDN and 0.1 mM TCEP).

Voltage clamp of NaDC3 activity in *Xenopus laevis* oocytes

For electrophysiology, NaDC3 complementary DNA (Genbank, 64849, courtesy of A. Pajor) was subcloned into pGEM-HE2 vector for heterologous expression in *X. laevis* oocytes (EcoCyte)[55] and confirmed by sequencing of the complete open reading frame. *X. laevis* oocytes were injected with 20 ng of complementary RNA coding for WT NaDC3 transcribed with the mMessage Machine kit (Ambion). After incubating the oocytes for 5 days at 17 °C, currents were measured using standard two-electrode voltage-clamp techniques (OC-725C; Warner Instruments) at room temperature. Experiments were performed in ND96 buffer (96 mM NaCl, 2 mM KCl, 5 mM HEPES, 1 mM $MgCl_2$ and 1.8 mM $CaCl_2$ at pH 7.6 with NaOH) supplemented with sodium succinate at indicated concentrations. Data were filtered at 1–3 kHz and digitized at 20 kHz using pClamp software (Molecular Devices). Microelectrode resistances were 0.1–0.5 MU when filled with 3 M KCl.

Whole-cell transport assay in HEK293 cells

HEK293 cells (American Type Culture Collection, CRL-1573) were seeded in either 24-well plates with around 120,000 cells or in 96-well plates with around 20,000 cells per well. The following day, Lipofectamine 3000 (Invitrogen) was used to transfect HEK293 cells with either pEGFP-NaDC3 or pEGFP vector. The transfections were performed according to the manufacturer's protocol, using 400 ng of DNA per well for a 24-well plate and 67 ng per well for a 96-well plate.

On day 2 after transfection, [^{3}H]succinate uptake experiments were performed and modeled on the basis of previously published studies of NaDC3 and NaCT[51,56]. Cells were briefly incubated in assay buffer containing 140 mM NaCl, 2 mM KCl, 1 mM $MgCl_2$, 1 mM $CaCl_2$ and 10 mM HEPES, with pH adjusted to 7.4 using 1 M Tris solution before uptake. All experiments were carried out at room temperature.

For the endpoint uptake experiments, the assay buffer was removed from 24-well plates and replaced with the uptake buffer, composed of the assay buffer supplemented with 15 nM [^{3}H]succinate (American Radiolabeled Chemicals, ART-1700) for a total of 15 µM succinate. The uptake buffer was removed after 15 min and cells were washed three times with 0.5 ml of ice-cold stopping buffer containing 140 mM choline chloride, 2 mM KCl, 1 mM $MgCl_2$, 1 mM $CaCl_2$ and 10 mM HEPES, with pH adjusted to 7.4 using 1 M Tris solution. The stopping buffer was completely aspirated and 0.5 ml of Ultima Gold XR scintillation cocktail (PerkinElmer, 6013111) was added and mixed on a rocker for 30 min to 1 h. Counts were measured using a Wallac 1450 MicroBeta liquid scintillation counter. For experiments with the inhibitor PF4a, cells were incubated overnight (~16 h) with varying concentrations of inhibitor ranging from 0 to 1,000 µM. They were briefly washed with assay buffer before the uptake was performed as above in the presence of the same varying PF4a concentrations.

The uptake kinetic experiments were conducted using a 96-well plate. The assay buffer was substituted with various concentrations of total succinate in the uptake buffer, from 100 to 0.5 µM, each supplemented with 0.05% [^{3}H]succinate. Uptake was terminated at intervals of 1, 2, 4 and 8 min by triple washing with 0.2 ml of ice-cold stopping buffer. Any delays were recorded. Following the washes, the buffer was completely aspirated and 0.2 ml of Ultima Gold XR scintillation cocktail was introduced and gently mixed on a rocker for 30 min before transferring the solutions to an Isoplate 96-well plate (PerkinElmer) for counting.

Data were evaluated using GraphPad Prism version 9.4.1. All datasets represented included values from 2–3 independent experiments performed in duplicates or triplicates. Michaelis–Menten kinetics were derived by plotting the initial uptake velocity, measured in counts per minute (CPM), against various substrate concentrations. The uptake velocity itself was determined through linear regression analysis of the uptake data during the initial 4-min period. An unpaired *t*-test was used to compare the succinate uptake of each NaDC3 phenylalanine mutant to the WT for statistical analysis of endpoint uptake assays. The PF4a datasets were normalized by scaling the mean values of the highest and lowest PF4a concentrations in each experiment between 0 and 1, respectively. Subsequently, a global four-parameter dose–response inhibition fit was applied to the datasets to determine the IC_{50} of PF4a to NaDC3.

Fluorescence microscopy

Fluorescence microscopy images were captured of HEK293 cells 2 days after transfection with pEGFP-NaDC3 WT and F93Y mutant. The imaging was carried out on a Nikon Eclipse Ti microscope with a ×40 objective (Plan Apo λ ×40, Nikon) and a digital camera (Hamamatsu) with an excitation wavelength of 490 nm.

NaDC3 substrates binding by tryptophan fluorescence quenching

Tryptophan fluorescence quenching was used to measure affinity of succinate, DMS and αKG to purified NaDC3 in detergent, following a protocol modified for other membrane transporters[43,45,57–60]. NaDC3 was purified by size-exclusion chromatography (SEC) in a buffer of 25 mM Tris pH 7.5, 100 mM NaCl, 10 mM succinate and 0.02% GDN. Immediately before use, protein was dialyzed four times for 20 min in SEC buffer without substrate at 4 °C with stirring. Protein was diluted to a final concentration of 1 µM in buffer containing 25 mM Tris pH 7.5, 100 mM NaCl and 0.02% GDN. Using a Horiba FluoroMax-4 fluorometer at 22 °C and a 280-nm excitation wavelength, the emission spectrum was recorded between 290 and 400 nm. The maximum was determined to be ~337 nm. Subsequently, the change in fluorescent emission at 337 nm was monitored with increasing concentrations of succinic acid pH 7.5, DMS or αKG (0.1 µM–1 mM substrate for succinate and DMS or 0.1 µM–2.5 mM for αKG).

Each wavelength scan was measured in triplicate for each substrate concentration. Each experimental condition was repeated three times for succinate and αKG and four times for DMS binding. The binding curve was fit in Prism using a site-specific binding equation to account for bound substrate, with error bars indicating the s.d.

Overexpression and purification of NaCT

Human *SLC13A5* was overexpressed and purified as previously described[43]. Briefly, *T. ni* BTI-Tn-5B1-4 cells were infected with a baculovirus containing the WT human *SLC13A5* gene with an N-terminal 10xHis tag. Cells were harvested and lysed in a buffer of 50 mM Tris pH 8.0, 400 mM NaCl, 10 mM lithium citrate and 10% glycerol. Membranes were isolated by ultracentrifugation and solubilized in a buffer of 50 mM Tris pH 8.0, 200 mM NaCl, 10 mM lithium citrate, 10% glycerol and 1.3% dodecyl-maltoside (Anatrace, D310). NaCT was subsequently purified on a Ni^{2+}-NTA affinity column and, after exchange to amphipol (PMAL-C8, Anatrace, P5008), a Superdex 200 10/300 GL size-exclusion column.

Cryo-EM specimen preparation

SEC-purified NaDC3 was concentrated with a 100-kDa centrifugal concentrator (Millipore). Following the addition of a substrate or inhibitor (20 mM lithium succinate, 20 mM αKG, 20 mM DMS or 200 μM PF4a (Sigma, PZ0318)), the sample was used immediately. For NaCT, 20 mM lithium succinate or 200 μM PF4a was added to protein purified in amphipol before grid freezing. All cryo-EM grids were prepared by applying 3.5 μl of protein solution at 6 mg ml^{-1} to a glow-discharged UltrAuFoil R1.2/1.3 300-mesh grid (Quantifoil, N1-A1nAu30-01) and blotted for 3–4 s under 100% humidity at 8 °C before plunging into liquid ethane using a Mark IV Vitrobot (Thermo Fisher Scientific).

Cryo-EM data collection and image processing

All cryo-EM imaging was performed under control of Leginon (version 3.6)[61]. Following screening on a 200-kV Talos Arctica equipped with a K3 camera, samples that could generate a map better than 6 Å were selected for data collection on a 300-kV Titan Krios microscope equipped with a K3 camera. As the use of thinner ice has been shown to be successful in increasing the signal-to-noise ratio and, thus, improving resolution[62–65], we measured the ice thickness on the fly[66,67], which allowed for the selection of holes with the desired ice thickness for data collection.

Datasets of NaDC3 in GDN in the presence of various substrates or inhibitors (succinate, αKG or PF4a) were collected from untilted grids. NaCT–succinate and NaCT–PF4a samples and NaDC3 in DMS displayed a preferred orientation on grids; thus, images were collected from both untilted and 40° tilted specimens[43]. Data acquisition was performed with an energy filter slit width of 20 eV, at a magnification of ×105,000, on a K3 direct electron detector with a pixel size of 0.4125 Å in super-resolution. Defocus values were set ranging from −0.8 to −1.6 μm. Leginon (version 3.6)[61,67] was used to target holes with 17–30 nm of ice alternatively measured by the zero loss peak and aperture-limited scattering as previously described[66]. On-the-fly data quality was measured by running MotionCor2 (version 1.5)[68] and CTFFIND4 (version 4.1.13)[69] under the control of Appion[70]. All images were acquired with image shifts up to 7 μm, with hardware beam tilt correction enabled in Leginon. Particles were picked on the fly using WARP[71] and two-dimensional (2D) classification was performed on the fly during screening using cryoSPARC (version 3.3.1)[72]. All particle polishing was performed in RELION 4.0 (ref. 73).

For NaDC3–succinate data collection, 5,179 videos were collected from 0° tilted specimens. Patch contrast transfer function (CTF) estimation in cryoSPARC was used for initial CTF estimation of the whole dataset. Micrographs with an overall resolution worse than 5 Å were excluded from subsequent steps. Selected particles from WARP (version 1.0.9) real-time picking and the correlated 2D classification results were used as input templates for Topaz[74] repicking or Template picking in cryoSPARC with a pixel size of 1.65 Å. After two rounds of 2D classification, selected particles underwent five rounds of heterogeneous three-dimensional (3D) refinement against three ab initio models generated from the selected WARP picking particles. After re-extracting particles with a pixel size of 0.825 Å, three rounds of heterogeneous 3D refinements were processed against the new ab initio models generated from the previous round of the new unbinned particle set. In this way, the 3D classification of the dataset generated two good classes, one in a C_{oo}–C_{oo} conformation and the other in a C_{oo}–C_i conformation. Another six rounds of heterogeneous 3D refinements were processed against the second round of ab initio models that were the best group to help separate the two conformations. A total of 202,740 particles resulting in a 2.54-Å C_{oo}–C_{oo} map and 228,347 particles resulting in a 2.61-Å C_{oo}–C_i map by nonuniform refinement were finally selected for particle polishing in RELION 4.0 (ref. 73). Finally, a local refinement in cryoSPARC was helpful in improving the map quality, resulting in the final C_{oo}–C_{oo} conformation map at a resolution of 2.53 Å and the final C_{oo}–C_i conformation map at a resolution of 2.60 Å (Extended Data Fig. 2).

For NaDC3–DMS data collection, 5,984 and 13,540 videos were collected from 0° and 40° tilted specimens, respectively. Following initial image processing steps performed similarly to the NaDC3–succinate dataset, 3D classification of this dataset generated two good classes: one in C_i–C_i as the main conformation and another in C_o–C_i as the minor conformation. Another six rounds of heterogeneous 3D refinements were processed against the third round of ab initio models that were the best group to help separate the two conformations. A total of 397,856 particles resulting in a 2.25-Å C_i–C_i map and 60,488 particles resulting in a 2.92-Å C_o–C_i map by nonuniform refinement were finally selected for particle polishing. Several rounds of higher-order CTF correction and nonuniform refinement were applied before the local refinement, resulting in the final map of the C_i–C_i conformation at a resolution of 2.17 Å.

For NaDC3–αKG data collection, 4,201 videos were collected from 0° tilted specimens. Following initial image processing steps performed similarly to the NaDC3–succinate dataset, only one good class was generated from the 3D classification of this dataset. Another six rounds of heterogeneous 3D refinements were processed against the best ab initio models. A total of 330,891 particles resulting in a 2.11-Å map by nonuniform refinement were finally selected for particle polishing. Several rounds of higher-order CTF correction and nonuniform refinement were applied before a local refinement resulted in a final map at a resolution of 2.09 Å.

For NaDC3–PF4a data collection, 2,558 and 4,221 micrographs were collected from 0° and 40° tilted specimens, respectively. Following initial image processing steps performed similarly to the NaDC3–succinate dataset, only one good class was generated from the 3D classification of this dataset. Another six rounds of heterogeneous 3D refinements were processed against the best ab initio models. A total of 476,543 particles resulting in a 2.33-Å map by nonuniform refinement were finally selected for particle polishing. Several rounds of higher-order CTF correction and nonuniform refinement were applied before a local refinement resulted in a final map at a resolution of 2.16 Å.

For NaCT–succinate data collection, 8,113 and 2,246 videos were collected from 0° and 40° tilted specimens, respectively. Following initial image processing steps performed similarly to the NaDC3–succinate dataset, only one good class was generated from the 3D classification of this dataset. Another six rounds of heterogeneous 3D refinements were processed against the best ab initio models. A total of 323,571 particles resulting in a 2.41-Å map by nonuniform refinement were finally selected for particle polishing. Several rounds of higher-order CTF correction and nonuniform refinement were applied before a local refinement, resulting in a final map at a resolution of 2.33 Å.

For NaCT–PF4a data collection, 9,030 and 3,515 videos were collected from 0° and 40° tilted specimens, respectively. Following initial image processing steps performed similarly to the NaDC3–succinate dataset, only one good class was generated from the 3D classification of this dataset. Another eight rounds of heterogeneous 3D refinements were processed against the best ab initio models. A total of 745,845 particles resulting in a 2.25-Å map by nonuniform refinement were finally selected for particle polishing. Several rounds of higher-order CTF correction and nonuniform refinement were applied before a local refinement, resulting in a final map at a resolution of 2.13 Å.

Model building and refinement

For NaDC3 model building, the predicted structure generated by AlphaFold2 (ref. 75) in a C_i conformation (Q8WWT9) was used as the initial structure model of NaDC3. All NaDC3 maps were aligned against the scaffold domain of the AlphaFold2-predicted NaDC3 structure. The model of transport domain in the AlphaFold2-predicted NaDC3 structure in a C_i conformation was used in model building of the transport domain by performing a rigid-body fitting to transform from the C_i to

the C_{oo} or C_o conformation. The coordinates of the linker helix and loops of NaDC3 were manually adjusted in Coot (version 0.9.6)[76].

For NaCT model building, the previous NaCT–citrate structure (Protein Data Bank (PDB) 7JSK)[43] was used as the initial structure model and the NaCT maps were aligned against the scaffold domain of the NaCT–citrate structure. The model of the scaffold domain in the NaCT–citrate structure was directly used in the C_i conformation model building. The model of the transport domain in the NaCT–citrate structure was used in the C_i conformation model building by performing a rigid-body fitting to the NaCT C_i conformation. The coordinates of the linker helix and loops of NaCT were manually adjusted in Coot. The substrate coordination of succinate, PF4a, αKG and DMS was drawn using Chemical Sketch (version 1.0)[77]. Ligand restraint files were generated from PHENIX (version 1.19)[78]. Each model was manually checked and modified using Coot and ISOLDE (version 1.0) in ChimeraX (version 1.4)[79,80], before finally being refined against the corresponding map using real-space refinement in PHENIX. All figures were prepared in ChimeraX and PyMol (version 2.5.2; Schrödinger)[81].

There is currently no knowledge on Li^+ affinity or its binding site(s) in NaDC3. As Li^+ inhibits NaDC3 transport activity[35,36] and can drive substrate transport in some homologous SLC13 and DASS proteins such as NaCT and VcINDY[4], it was assumed that Li^+ occupies the same cation sites as Na^+. Therefore, the density observed at the cation sites in our cryo-EM maps likely contains contributions from both Na^+ and Li^+, making the Na^+ densities weaker and their positions less well defined.

In addition to the protein and ligands, we tentatively fitted cholesterol and phosphatidylcholine into the previously unaccounted for density in the six maps of NaDC3 in GDN. The two NaCT maps in amphipol did not contain any lipids. It is possible that the GDN better preserves cholesterol and lipids associated with the transporters. The role of such cholesterol and lipids remains unknown.

NMR spectroscopy measurements

Solution ^{1}H-NMR spectra of PF4a (PZ0318, Sigma) were recorded at 298 K on a Bruker spectrometer operating at a ^{1}H frequency of 800 MHz equipped with a triple-resonance TCI cryogenic probe at the Shared Instrument Facility of Department of Chemistry, New York University (NYU). The sample was dissolved in DMSO-d_6 (ref. 34). Spectra were processed using Topspin 4.1.1. The spectra were calibrated relative to residual undeuterated solvent signal at 2.508 ppm.

Reporting summary

Further information on research design is available in the Nature Portfolio Reporting Summary linked to this article.

Data availability

EM densities and protein models were deposited to the EM Data Bank and PDB for the NaDC3–succinate C_{oo}–C_{oo} (EMD-42621, 8UVI), NaDC3–succinate C_{oo}–C_i (EMD-42617, 8UVE), NaDC3–DMS C_o–C_i (EMD-42619, 8UVG), NaDC3–DMS C_i–C_i (EMD-42618, 8UVF), NaDC3–αKG C_i–C_i (EMD-42615, 8UVC), NaDC3–PF4a C_i–C_i (EMD-42616, 8UVD), NaCT–succinate C_i–C_i (EMD-42620, 8UVH) and NaCT–PF4a C_i–C_i (EMD-42614, 8UVB) complexes. Source data are provided with this paper.

References

54. Superti-Furga, G. et al. The RESOLUTE consortium: unlocking SLC transporters for drug discovery. *Nat. Rev. Drug Discov.* **19**, 429–430 (2020).
55. Liman, E. R., Tytgat, J. & Hess, P. Subunit stoichiometry of a mammalian K^+ channel determined by construction of multimeric cDNAs. *Neuron* **9**, 861–871 (1992).
56. Kaufhold, M. et al. Differential interaction of dicarboxylates with human sodium–dicarboxylate cotransporter 3 and organic anion transporters 1 and 3. *Am. J. Physiol. Renal Physiol.* **301**, F1026–F1034 (2011).
57. Boulter, J. M. & Wang, D. N. Purification and characterization of human erythrocyte glucose transporter in decylmaltoside detergent solution. *Prot. Expr. Purif.* **22**, 337–348 (2001).
58. Li, X. D. et al. Monomeric state and ligand binding of recombinant GABA transporter from *Escherichia coli*. *FEBS Lett.* **494**, 165–169 (2001).
59. Auer, M. et al. High-yield expression and functional analysis of *Escherichia coli* glycerol-3-phosphate transporter. *Biochemistry* **40**, 6628–6635 (2001).
60. Law, C. J., Yang, Q., Soudant, C., Maloney, P. C. & Wang, D. N. Kinetic evidence is consistent with the rocker-switch mechanism of membrane transport by GlpT. *Biochemistry* **46**, 12190–12197 (2007).
61. Suloway, C. et al. Automated molecular microscopy: the new Leginon system. *J. Struct. Biol.* **151**, 41–60 (2005).
62. Wu, M. & Lander, G. C. How low can we go? Structure determination of small biological complexes using single-particle cryo-EM. *Curr. Opin. Struct. Biol.* **64**, 9–16 (2020).
63. Sauer, D. B. et al. Structural basis for the reaction cycle of DASS dicarboxylate transporters. *eLife* **9**, e61350 (2020).
64. Neselu, K. et al. Measuring the effects of ice thickness on resolution in single particle cryo-EM. *J. Struct. Biol. X* **7**, 100085 (2023).
65. Zheng, L. et al. Uniform thin ice on ultraflat graphene for high-resolution cryo-EM. *Nat. Methods* **20**, 123–130 (2023).
66. Rice, W. J. et al. Routine determination of ice thickness for cryo-EM grids. *J. Struct. Biol.* **204**, 38–44 (2018).
67. Cheng, A. et al. Leginon: new features and applications. *Protein Sci.* **30**, 136–150 (2021).
68. Zheng, S. Q. et al. MotionCor2: anisotropic correction of beam-induced motion for improved cryo-electron microscopy. *Nat. Methods* **14**, 331–332 (2017).
69. Rohou, A. & Grigorieff, N. CTFFIND4: fast and accurate defocus estimation from electron micrographs. *J. Struct. Biol.* **192**, 216–221 (2015).
70. Lander, G. C. et al. Appion: an integrated, database-driven pipeline to facilitate EM image processing. *J. Struct. Biol.* **166**, 95–102 (2009).
71. Tegunov, D. & Cramer, P. Real-time cryo-electron microscopy data preprocessing with Warp. *Nat. Methods* **16**, 1146–1152 (2019).
72. Punjani, A., Rubinstein, J. L., Fleet, D. J. & Brubaker, M. A. cryoSPARC: algorithms for rapid unsupervised cryo-EM structure determination. *Nat. Methods* **14**, 290–296 (2017).
73. Zivanov, J. et al. A Bayesian approach to single-particle electron cryo-tomography in RELION-4.0. *eLife* **11**, e83724 (2022).
74. Bepler, T. et al. Positive-unlabeled convolutional neural networks for particle picking in cryo-electron micrographs. *Nat. Methods* **16**, 1153–1160 (2019).
75. Jumper, J. et al. Highly accurate protein structure prediction with AlphaFold. *Nature* **596**, 583–589 (2021).
76. Emsley, P. & Cowtan, K. Coot: model-building tools for molecular graphics. *Acta Crystallogr. D* **60**, 2126–2132 (2004).
77. Berman, H. M. et al. The Protein Data Bank. *Nucleic Acids Res.* **28**, 235–242 (2000).
78. Liebschner, D. et al. Macromolecular structure determination using X-rays, neutrons and electrons: recent developments in PHENIX. *Acta Crystallogr. D* **75**, 861–877 (2019).
79. Croll, T. I. ISOLDE: a physically realistic environment for model building into low-resolution electron-density maps. *Acta Crystallogr. D* **74**, 519–530 (2018).
80. Meng, E. C. et al. UCSF ChimeraX: tools for structure building and analysis. *Protein Sci.* **32**, e4792 (2023).
81. DeLano, W. L. *The PyMOL User's Manual, 1* (DeLano Scientific, 2002).

Acknowledgements
D.-N.W. was financially supported by the National Institutes of Health (NIH; R01NS108151, R01DK135088, R01AI165782 and R01GM121994), the G. Harold and Leila Y. Mathers Foundation and the TESS Research Foundation. V.M. and J.A.M. were supported by the National Institute of Neurological Disorders and Stroke intramural program. R. Mancusso and F. Ono made initial efforts in expressing the proteins. We thank the following colleagues for reagents, technical assistance and helpful discussions: M. Bauerle, N. Coudray, J. Li, A. Pajor and M. Sweet. The NYU Cryo-EM Core Laboratory (RRID: SCR_019202) is partially supported by the Laura and Isaac Perlmutter Cancer Center support grant from the NIH and National Cancer Institute (P30CA016087). Additional screening was performed at the Simons EM Center at the New York Structural Biology Center, funded with major support from the Simons Foundation (SF349247), where we acknowledge J. Wang for assistance. EM data processing used computing resources at the high-performance computing facility of the NYU Langone Medical Center and we were assisted by K. Yie, A. Siavosh-Haghighi and M. Costantino. We are grateful to J. Li and C. Lin from the Department of Chemistry, NYU for NMR spectrum data measurements.

Author contributions
Y.L. froze grids, collected cryo-EM images, processed the images and built the atomic models. J.S. developed expression and purification systems and prepared protein samples. V.M., A.B. and J.A.M. conducted whole-cell activity studies. J.J.M. carried out substrate-binding measurements. H.K., B.W. and W.J.R. collected cryo-EM images. W.J.R. provided advice on image processing. Y.L. and D.-N.W. analyzed the structures and wrote the paper. All authors participated in the discussion and paper editing. D.-N.W. supervised the research.

Competing interests
The authors declare no competing interests.

Additional information
Extended data is available for this paper at https://doi.org/10.1038/s41594-024-01433-0.

Supplementary information The online version contains supplementary material available at https://doi.org/10.1038/s41594-024-01433-0.

Correspondence and requests for materials should be addressed to Joseph A. Mindell or Da-Neng Wang.

Peer review information *Nature Structural & Molecular Biology* thanks Avner Schlessinger, Daniel Wacker and the other, anonymous, reviewer(s) for their contribution to the peer review of this work. Peer reviewer reports are available. Primary Handling Editor: Katarzyna Ciazynska, in collaboration with the *Nature Structural & Molecular Biology* team.

https://doi.org/10.1038/s41594-024-01433-0

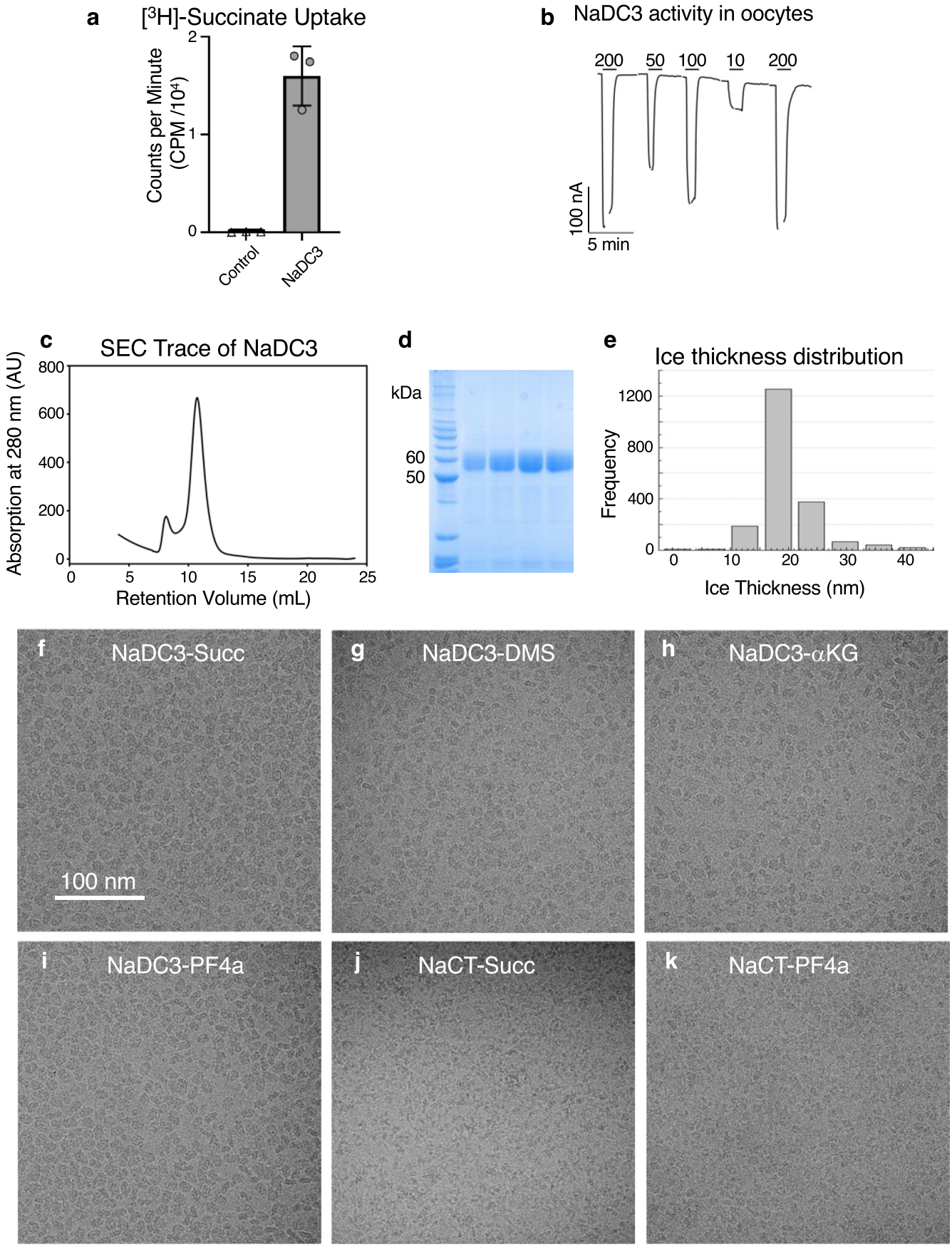

Extended Data Fig. 1 | See next page for caption.

https://doi.org/10.1038/s41594-024-01433-0

Extended Data Fig. 1 | Sample preparation and cryo-EM data collection of the human NaDC3 and NaCT proteins. a, [^{3}H]-succinate uptake by NaDC3 in HEK293 cells ($N = 3$). Cells transfected with an empty vector were used as a control. Results of individual experiments are shown as points, with each point an average of three biological replicates. Error bars depict the standard deviation (SD). **b**, Two-electrode-voltage-clamp recordings of NaDC3 expressed in *Xenopus* oocytes. A representative recording of NaDC3 exposed to a range of succinate concentrations (bars) as indicated. Gaps indicate pauses in recording protocol to obtain other data. These results show that the designed constructs were active. **c**, SEC trace of NaDC3 purification in LiCl, NaCl and detergent GDN. **d**, Representative SDS-PAGE of purified NaDC3. The experiments were repeated over ten times. **e**, On-the-fly ice thickness measurements of cryo-EM grids of NaDC3 samples. Grid holes with ice thickness in the range of 17 – 30 nm were selected for data collection. Cryo-electron micrographs of various samples: **f**, NaDC3-Succ; **g**, NaDC3-DMS; **h**, NaDC3-αKG; **i**, NaDC3-PF4a; **j**, NaCT-Succ; **k**, NaCT-PF4a. All the electron micrographs in (**f**-**k**) are shown at the same magnification. Each micrograph is a representative of 5,000 – 20,000 individually recorded electron micrograph movies.

https://doi.org/10.1038/s41594-024-01433-0

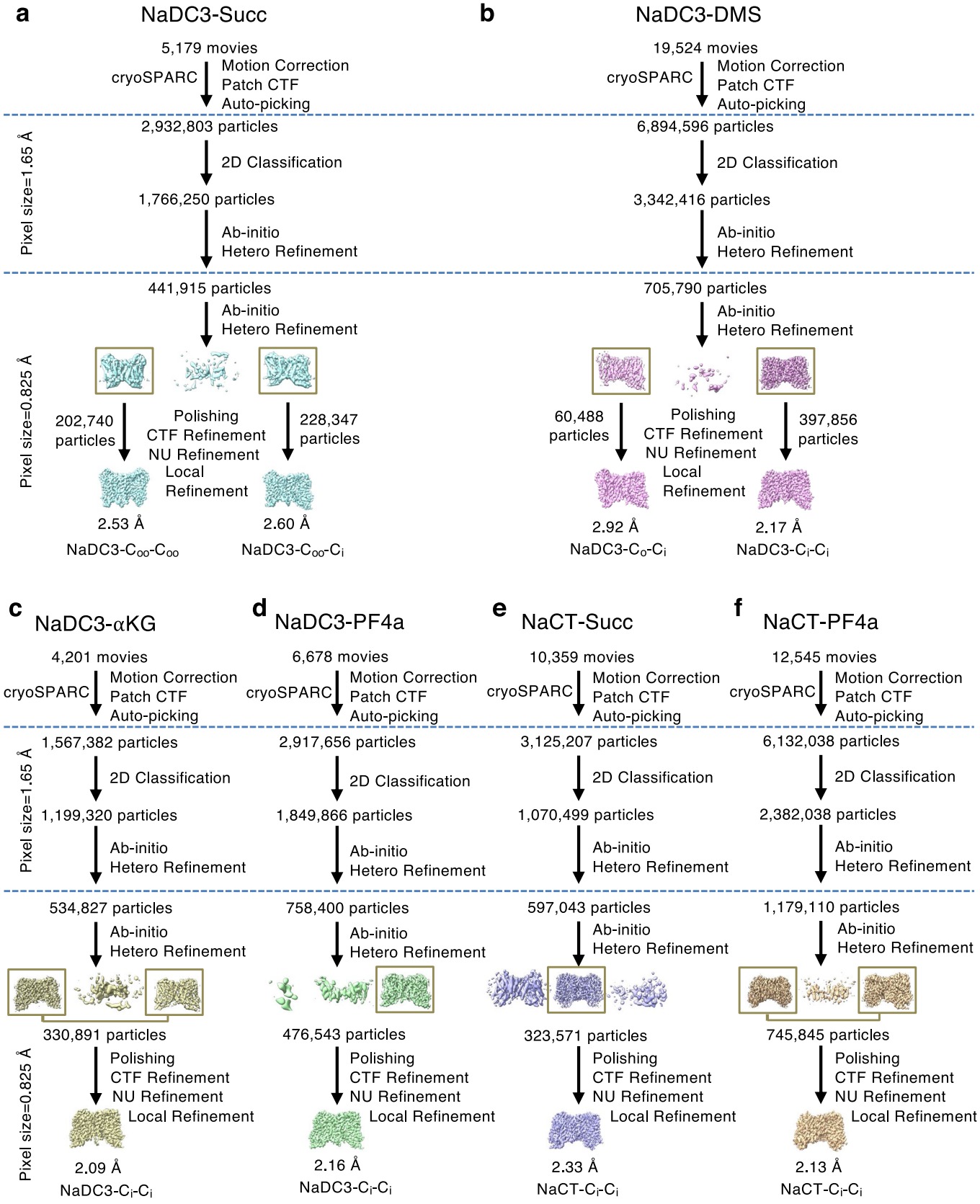

Extended Data Fig. 2 | Flow chart of image processing of NaDC3 and NaCT datasets. Flow chart of image processing strategy for various cryo-EM datasets: **a**, NaDC3-Succ; **b**, NaDC3-DMS; **c**, NaDC3-αKG; **d**, NaDC3-PF4a; **e**, NaCT-Succ; **f**, NaCT-PF4a.

https://doi.org/10.1038/s41594-024-01433-0

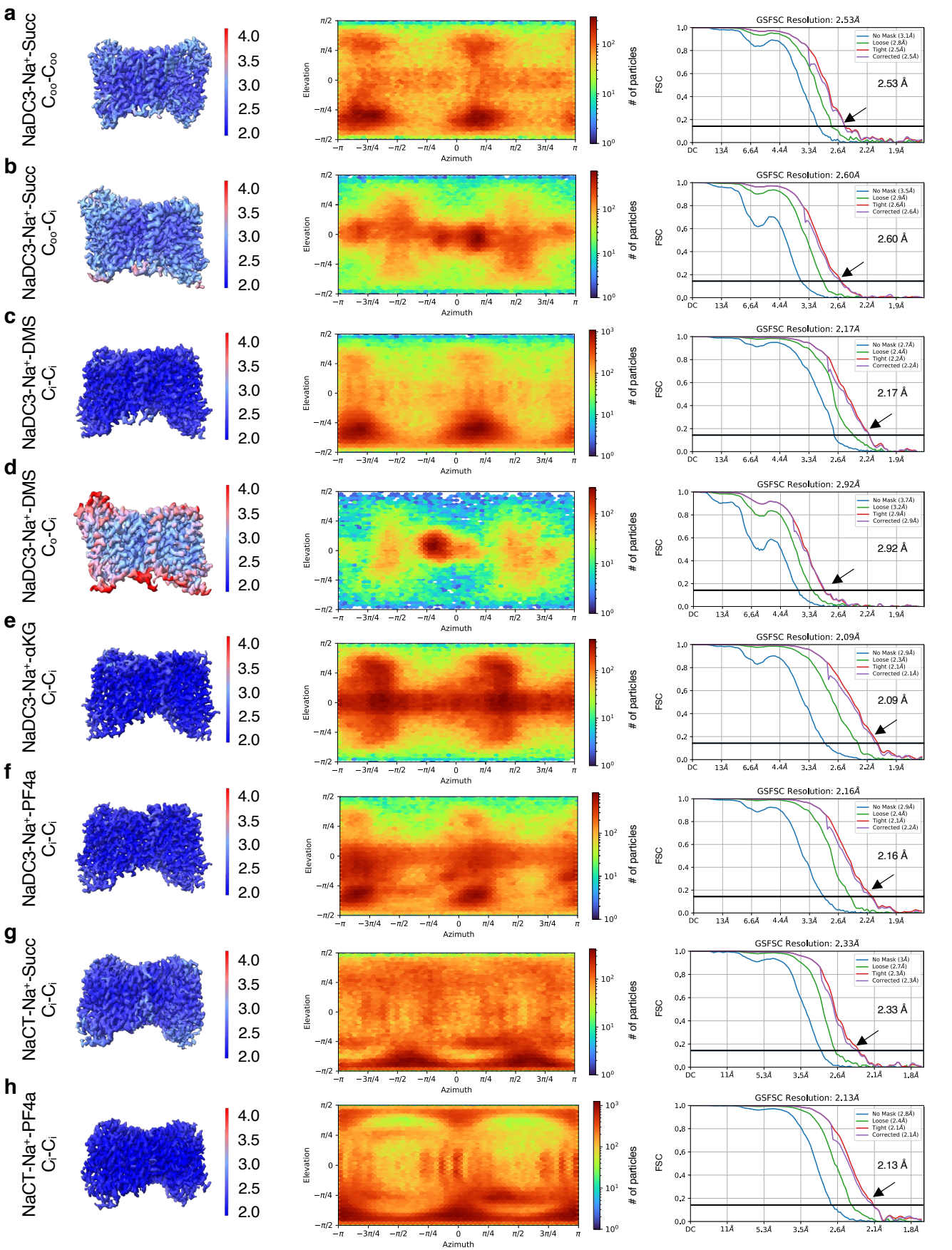

Extended Data Fig. 3 | See next page for caption.

https://doi.org/10.1038/s41594-024-01433-0

Extended Data Fig. 3 | Cryo-EM analysis of NaDC3 and NaCT datasets. Local resolution cryo-EM map (left), angular distribution of particles used for the final 3D reconstructions (middle), and gold-standard Fourier Shell Correlation (FSC) curves between the final two half maps (right) of various NaDC3 and NaCT maps: **a**, NaDC3-Succ, C_{oo}-C_{oo} dimer; **b**, NaDC3-Succ, C_{oo}-C_i dimer; **c**, NaDC3-DMS, C_o-C_i dimer; **d**, NaDC3-DMS, C_i-C_i dimer; **e**, NaDC3-αKG, C_i-C_i dimer; **f**, NaDC3-PF4a, C_i-C_i dimer; **g**, NaCT-Succ, C_i-C_i dimer; **h**, NaCT-PF4a, C_i-C_i dimer. Corrected FSC=0.143 positions are indicated by arrows.

https://doi.org/10.1038/s41594-024-01433-0

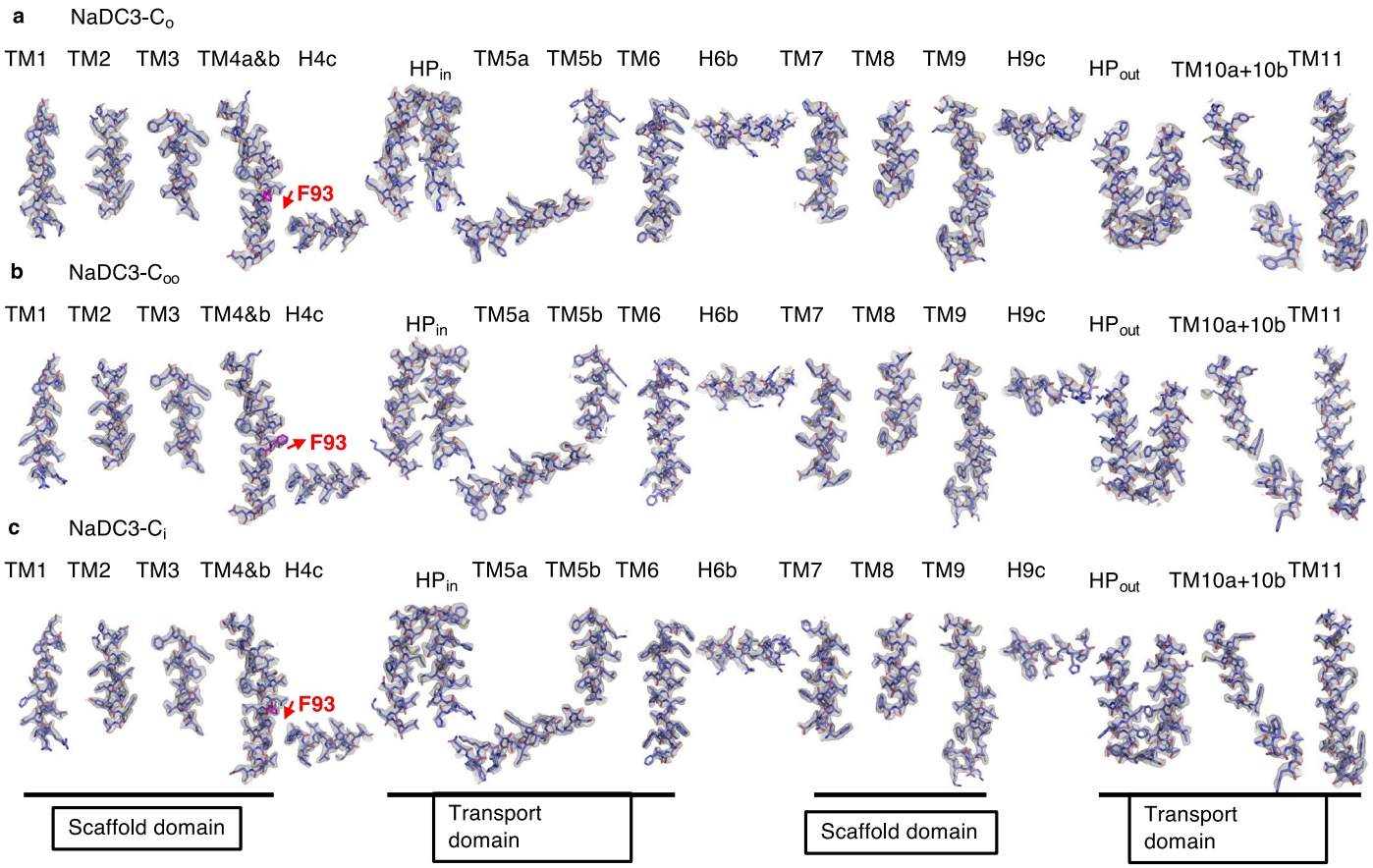

Extended Data Fig. 4 | Cryo-EM densities of NaDC3 in Co, Coo and Ci conformations showing the quality of chain tracing. Representative cryo-EM densities in various NaDC3 maps: **a**, C_o protomer in NaDC3-DMS C_o-C_i dimer; **b**, C_{oo} protomer in NaDC3-Succ C_{oo}-C_{oo} dimer; **c**, C_i protomer in NaDC3-DMS C_o-C_i dimer. The direction of the Phe93 side chain in each figure is indicated by an arrow.

https://doi.org/10.1038/s41594-024-01433-0

a Summary of NaDC3 and NaCT structures determined in this work

Protein complex	NaDC3-Succ		NaDC3-DMS		NaDC3-αKG	NaDC3-PF4a	NaCT-Succ	NaCT-PF4a
Dimer conformation*	C_{oo}-C_{oo}	C_{oo}-C_i	C_o-C_i	C_i-C_i	C_i-C_i	C_i-C_i	C_i-C_i	C_i-C_i
Ligand observed in the map	Succ/ Succ	Succ/ Succ	DMS/-	-/-	αKG/αKG (Up, Down)	PF4a/ PF4a (Rotamer-1, Rotamer-2)	-/-	PF4a/ PF4a
Resolution (Å)	2.53	2.60	2.92	2.17	2.09	2.16	2.33	2.13

*: C_o: outward-open conformation; C_{oo}: outward-facing, occluded conformation; C_i: inward-open conformation
Succ: succinate; DMS: 2,3-dimethylsuccinate; αKG: α-ketoglutarate; PF4a: PF-06761281 *R* enantiomer; -: no ligand density was observed in the cryo-EM map.

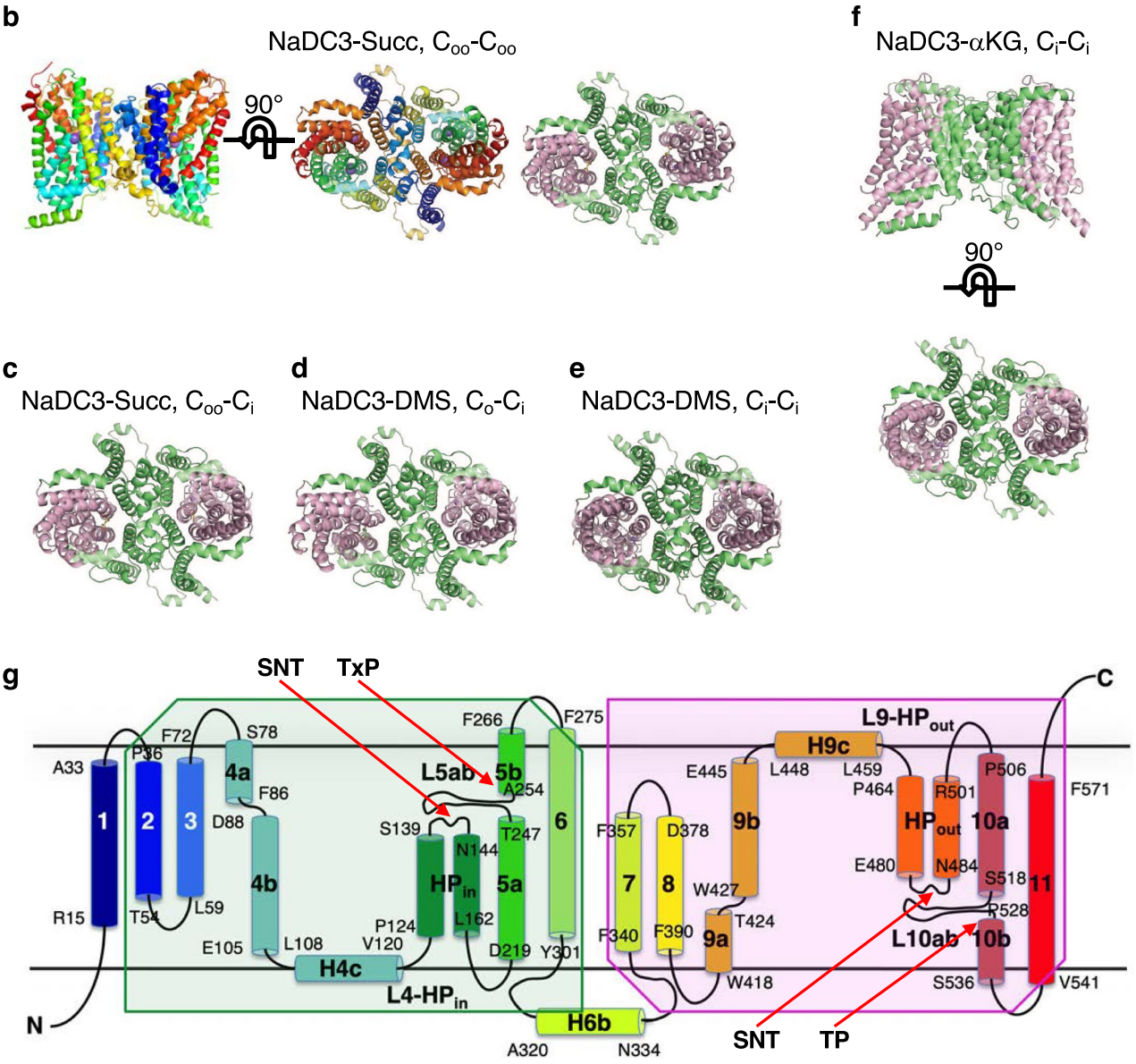

Extended Data Fig. 5 | See next page for caption.

https://doi.org/10.1038/s41594-024-01433-0

Extended Data Fig. 5 | Structures of NaDC3 and NaCT in the presence of different substrates and inhibitors. a, Summary of structures of NaDC3 and NaCT determined in the presence of various substrates and inhibitors. **b**, Structure of NaDC3-Succ, C_{oo}-C_{oo}. Left: viewed from within the membrane; middle and right: viewed from the extracellular space. The helices in the left and middle panels are colored in rainbow as in the sequence, while the scaffold and transport domains in the right panel are colored green and pink, respectively. **c**, Structure of NaDC3-Succ, C_{oo}-C_i dimer. **d**, Structure of NaDC3-DMS, C_o-C_i dimer. **e**, Structure of NaDC3-DMS, C_i-C_i dimer. **c**-**e** are viewed from the extracellular space. **f**, Structure of NaDC3-αKG, C_i-C_i dimer, viewed from within the membrane and from the extracellular space. **g**, Transmembrane topology of NaDC3. Amino acids at the beginning and end of each helix are indicated. The tips of hairpins HP_{in} and HP_{out} each contain an SNT motif, whereas the TxP and TP motifs are located at the N-termini of TM5b and TM10b, respectively.

https://doi.org/10.1038/s41594-024-01433-0

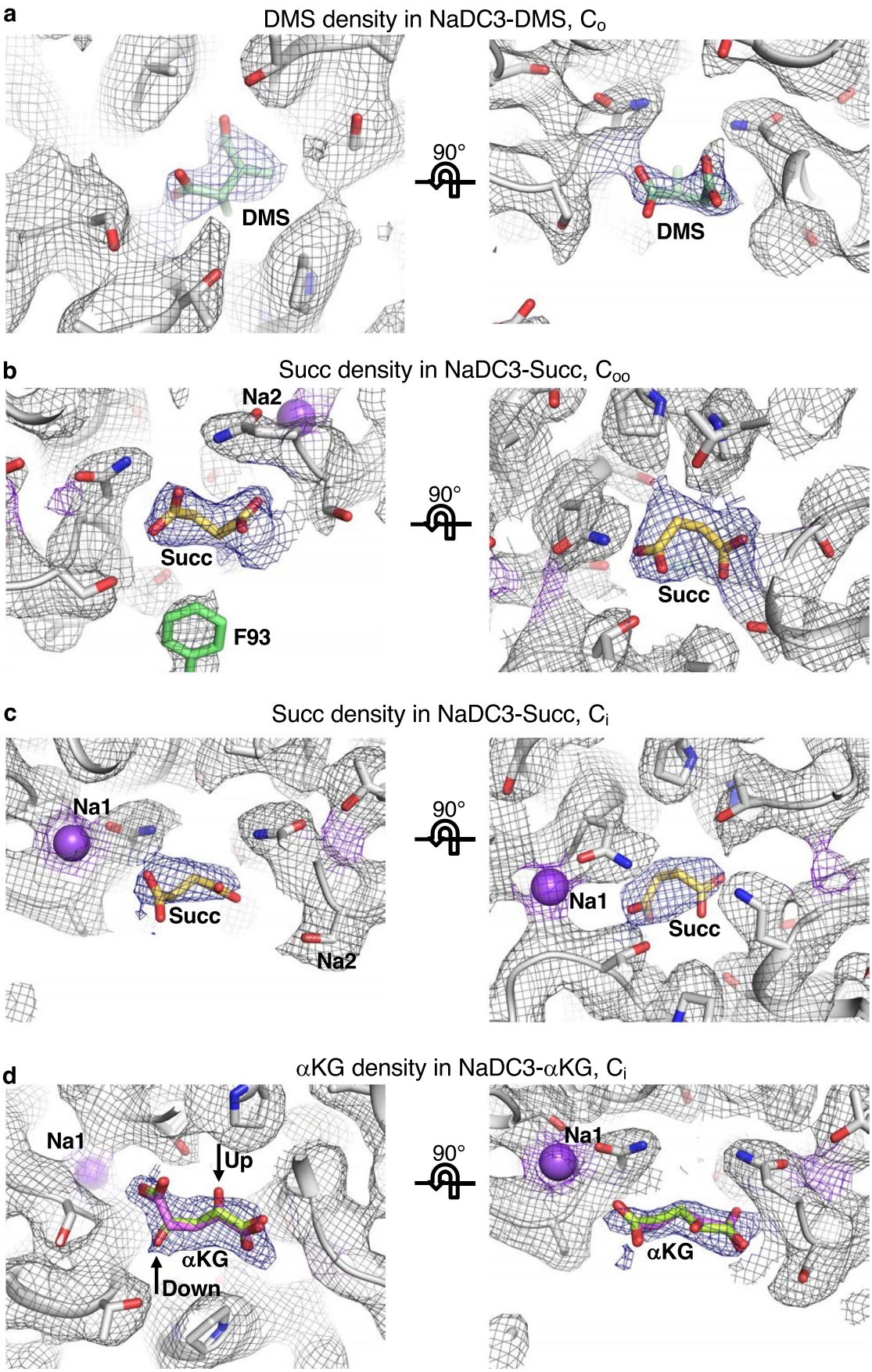

Extended Data Fig. 6 | See next page for caption.

https://doi.org/10.1038/s41594-024-01433-0

Extended Data Fig. 6 | Cryo-EM maps of NaDC3 determined in various substrates at the binding sites. The density maps along with each model are shown in two views, at a 90° rotation from each other. **a**, Cryo-EM density at the substrate site for the NaDC3-DMS, C_o conformation in C_o-C_i dimer. The densities for the protein (grey) and the substrate (blue) are both contoured at 4.5σ, respectively. **b**, Cryo-EM density at the substrate site for the NaDC3-Succ, C_{oo} conformation in C_{oo}-C_{oo} dimer. In addition to residues from the transport domain, Phe93 (green) from the scaffold domain also makes direct contact with the bound succinate (4 Å distance). The densities for the protein and the substrate are contoured at 7σ. **c**, Cryo-EM density at the substrate site for the NaDC3-Succ, C_i conformation in C_{oo}-C_i dimer. In this conformation, Phe93 is 6.1 Å away from the bound substrate. The densities for the protein and the substrate are contoured at 5σ. **d**, Cryo-EM density at the substrate site for the NaDC3-αKG, C_i conformation in C_i-C_i dimer. The arrows indicate the hydroxyl groups of the Up (yellow) and Down (light pink) conformers of the bound αKG. The densities for the protein and the substrate are contoured at 4.5σ.

https://doi.org/10.1038/s41594-024-01433-0

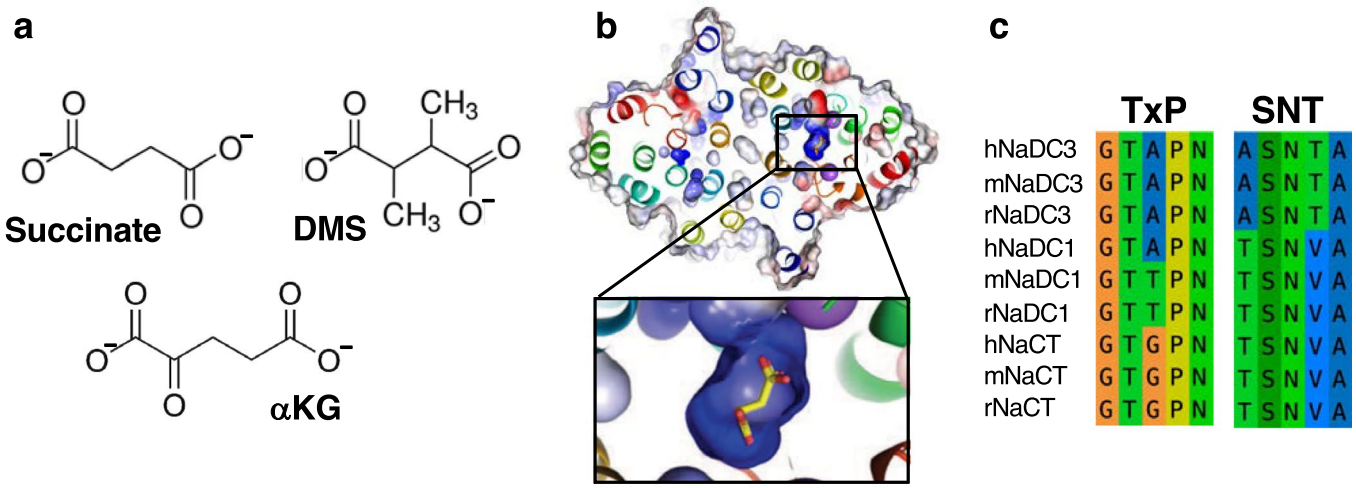

d Disease-causing mutations in NaDC3

	Mutations	Possible effects	References
Truncations (Blue)	Arg111	Misfolded protein.	(19)
Deletions (Orange)	ΔVal345 ΔLeu389		(19)
Missense mutations (Red)	Leu27Arg Thr62Met Pro58Leu Ala254Asp Pro493Leu Gly548Ser	-The Ala254Asp mutation occurs in the substrate site, and may therefore directly affect substrate binding. -Those mutations occur in the scaffold domain are likely to destabilize the protein.	(18,19)

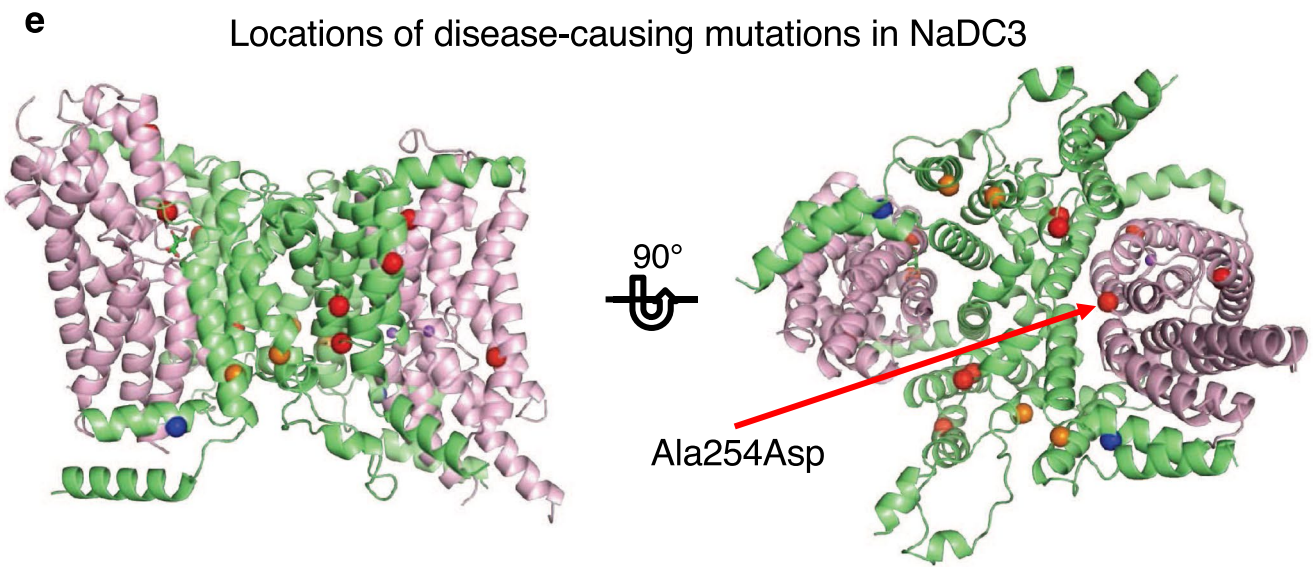

Extended Data Fig. 7 | See next page for caption.

https://doi.org/10.1038/s41594-024-01433-0

Extended Data Fig. 7 | Substrate binding site in NaDC3 and disease-causing mutations. a, Molecular structures of substrates of NaDC3, succinate (Succ), 2,3-dimethylsuccinate (DMS) and α-ketoglutarate (αKG). **b**, Electrostatic surface of the substrate binding pocket, C_{oo} conformation in C_{oo}-C_{oo} dimer. **c**, Amino acid sequence alignment of residues in the substrate binding pocket between NaDC3, NaDC1 and NaCT from human, mouse and rat. The sequences in the pocket are conserved except in the TxP motif in the N-terminal half, where the x can be an Ala, Thr or Gly, and the second SNT motif in the C-terminal half, where the threonine is a valine in NaDC1 and NaCT. **d**, Known mutations that cause acute reversible leukoencephalopathy. **e**, Mapping of the disease-causing mutations to the NaDC3 C_o-C_i structure. Early-termination, deletion and missense mutations are colored blue, orange and red, respectively. Ala254Asp (indicated by red arrow) occurs in the substrate binding pocket and likely abolishes dicarboxylate binding. Those mutations occur in the scaffold domain (green) are likely to destabilize the protein.

https://doi.org/10.1038/s41594-024-01433-0

a Domains in a NaDC3 protomer

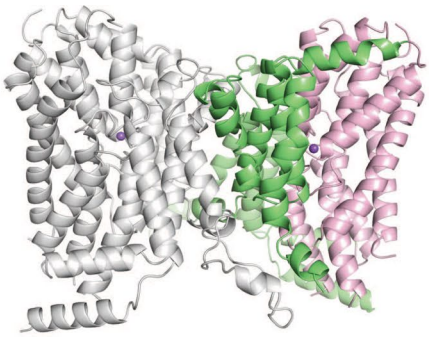

b r.m.s.d. of the NaDC3 scaffold domain

	C_o in C_o.C_i NaDC3-DMS	C_{oo} in C_{oo}.C_i NaDC3-Succ	C_i in C_{oo}.C_i NaDC3-Succ
C_o in C_o.C_i NaDC3-DMS			
C_{oo} in C_{oo}.C_i NaDC3-Succ	0.488 Å 237 AAs		
C_i in C_{oo}.C_i NaDC3-Succ	0.407 Å 210 AAs	0.519 Å 217 AAs	

c r.m.s.d. of the NaDC3 scaffold domain dimer

	C_o-C_i dimer NaDC3-DMS	C_{oo}-C_{oo} dimer NaDC3-Succ	C_{oo}-C_i dimer NaDC3-Succ	C_i-C_i dimer NaDC3-DMS
C_o-C_i dimer NaDC3-DMS				
C_{oo}-C_{oo} dimer NaDC3-Succ	0.550 Å 448 AAs			
C_{oo}-C_i dimer NaDC3-Succ	0.277 Å 480 AAs	0.471 Å 454 AAs		
C_i-C_i dimer NaDC3-DMS	0.411 Å 447 AAs	0.732 Å 443 AAs	0.339 Å 417 AAs	

d NaDC3-DMS, C_o v.s. NaDC3-Succ, C_{oo}

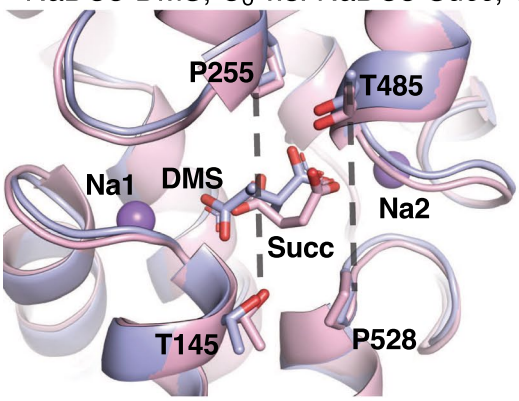

e NaDC3-Succ, C_{oo} v.s. NaDC3-Succ, C_i

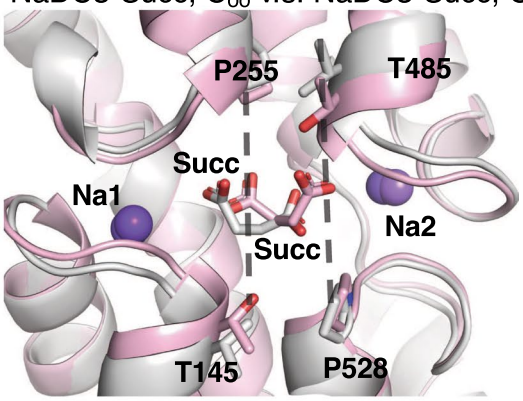

f r.m.s.d. of the NaDC3 transport domain

	C_o in C_o.C_i NaDC3-DMS	C_{oo} in C_{oo}.C_i NaDC3-Succ	C_i in C_{oo}.C_i NaDC3-Succ
C_o in C_o.C_i NaDC3-DMS			
C_{oo} in C_{oo}.C_i NaDC3-Succ	0.535 Å 228 AAs		
C_i in C_{oo}.C_i NaDC3-Succ	0.672 Å 218 AAs	0.694 Å 219 AAs	

g B-factor of NaDC3-Succ, C_{oo} – C_i dimer

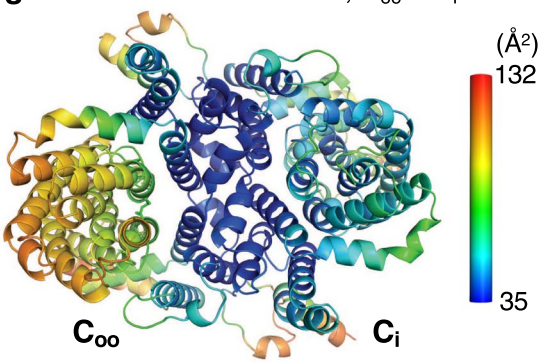

Extended Data Fig. 8 | See next page for caption.

https://doi.org/10.1038/s41594-024-01433-0

Extended Data Fig. 8 | Structural comparison of the scaffold domain and transport domain in NaDC3 in various conformations. a, Scaffold (light green) and transport (light pink) domains in a NaDC3 protomer, viewed from within the membrane plane. The other protomer in the dimer is shown in grey. The C_{oo}-C_{oo} dimer is shown here, but the domain organization is the same in all other conformations. **b**, r.m.s.d. comparison of the NaDC3 scaffold domain in C_o, C_{oo} and C_i conformations. **c**, r.m.s.d. comparison of the NaDC3 scaffold domain dimers between C_o-C_i, C_{oo}-C_{oo}, C_{oo}-C_i and C_i-C_i conformations. **d**, Structural comparison of the substrate site in the C_o conformation (NaDC3-DMS, light blue) and in the C_{oo} conformation (NaDC3-Succ, light pink). From the C_o to the C_{oo} conformations, the substrate site becomes more compact. The distances for Pro255-Thr145 and Thr485-Pro528 decrease from 10.3 Å and 10.5 Å to 9.4 Å and 9.7 Å, respectively. **e**, Structural comparison of the substrate site in the C_{oo} (light pink) and C_i (light grey) conformations in NaDC3-Succ dimer. From the occluded C_{oo} to the open C_i, the substrate site becomes more relaxed along the membrane normal. The distances between Pro255 and Thr145, and between Thr485 and Pro528, are increased from 9.8 Å to 11.6 Å, and from 9.8 Å to 11.8 Å, respectively. **f**, r.m.s.d. comparison of the transport domain in C_o, C_{oo} and C_i conformations. **g**, B-factor mapped onto the structure of the NaDC3-Succ, C_{oo}-C_i asymmetric dimer, viewed from the extracellular space.

https://doi.org/10.1038/s41594-024-01433-0

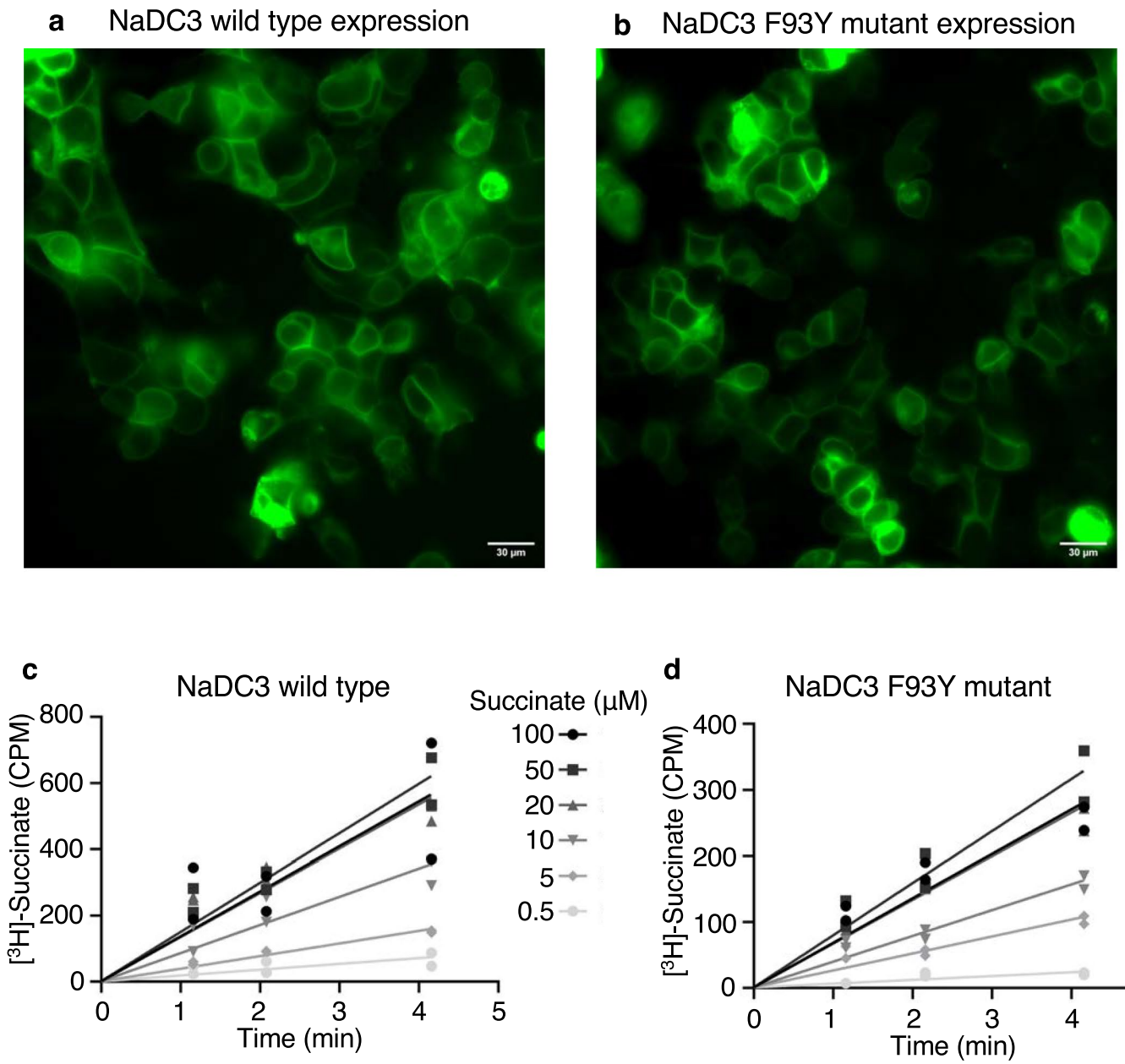

Extended Data Fig. 9 | Transport activity measurements of wild-type NaDC3 and Phe93Tyr mutant. Representative fluorescence micrographs showing the expression levels of NaCT-GFP in HEK293 cells, wild-type (**a**) and its Phe93Tyr mutant (**b**). At least four transfection experiments were carried out for each construct. Comparable amounts of the proteins are trafficked to the plasma membrane. Images were taken 48 hours post-transfection. Scale bars represent 30 µm. **c, d**, Representative graphs of initial [^{3}H]-succinate uptake by HEK293 cells expressing GFP-tagged NaDC3 wild-type (**c**) and its Phe93Tyr mutant variant (**d**) (N = 4). The X-axis shows the time since succinate addition (min), and the Y-axis the counts per minute (CPM) of [^{3}H]-succinate. Points indicate duplicate individual trials performed with separate samples transfected simultaneously. Lines represent linear regressions fit to all timepoints from a given concentration. Each graph depicts duplicates from a single experiment at each concentration and time point. Each graph represents a single biological replicate: results from two such replicates for each protein are shown in Fig. 5c, d.

https://doi.org/10.1038/s41594-024-01433-0

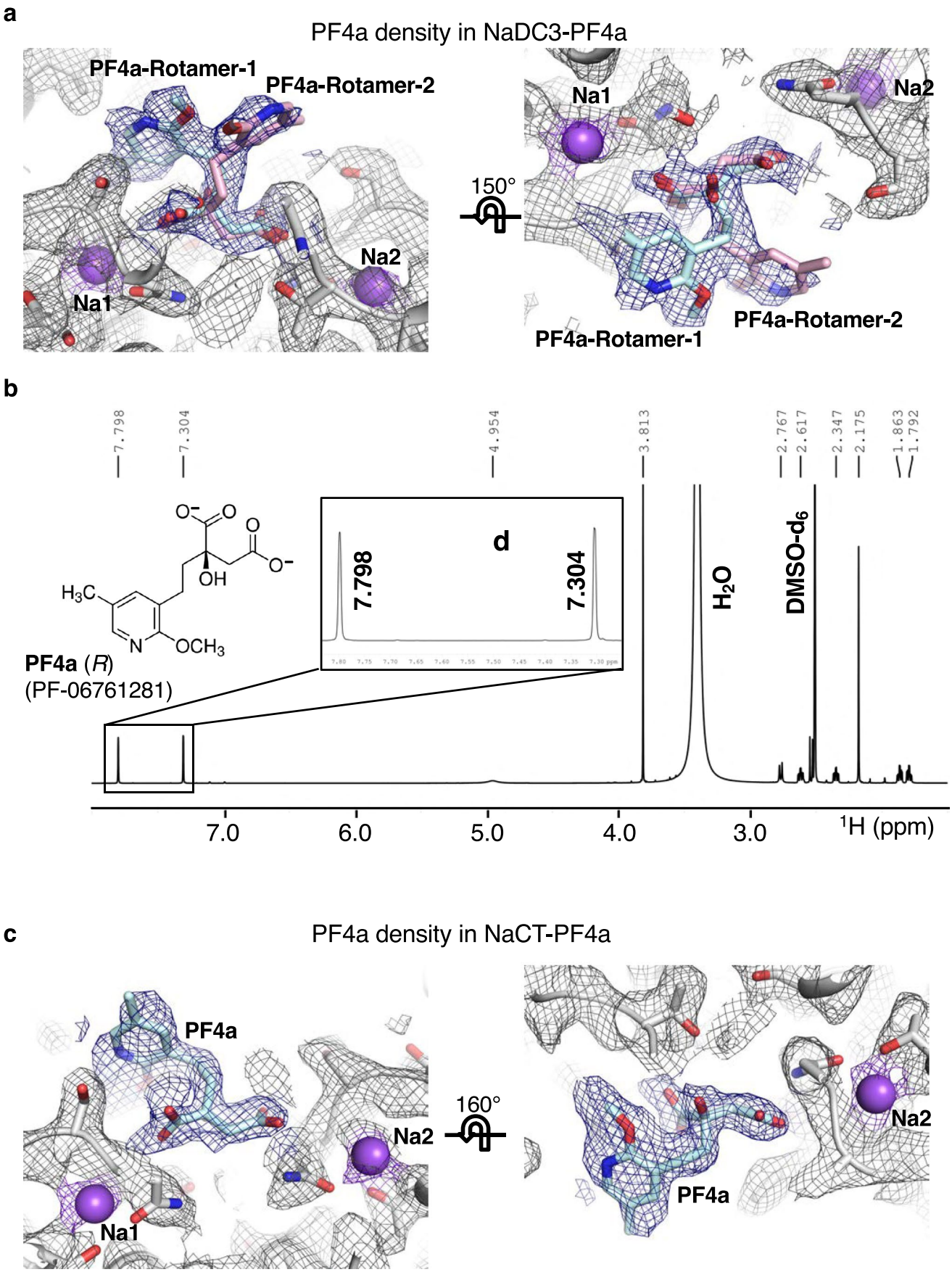

Extended Data Fig. 10 | See next page for caption.

https://doi.org/10.1038/s41594-024-01433-0

Extended Data Fig. 10 | Cryo-EM structures of NaDC3-PF4a and NaCT-PF4a complexes. a, Cryo-EM density at the PF4a site observed in NaDC3. The dicarboxylate moiety occupies the same location as a substrate, but two lobes of densities are found for the pyridine ring. The densities observed in the cryo-EM are two rotamers of the same compound, which we named Rotamer-1 (light blue) and Rotamer-2 (light pink). Two views of the binding site are shown. The densities for the protein (grey) and the inhibitor (blue) are both contoured at 5σ. **b**, 1D ^{1}H NMR spectra of the PF4a compound from Sigma measured in DMSO-d_6. The spectra are similar to those published for the pure *R*-form of the inhibitor molecule (Reference #34), supporting the above interpretation. The molecular structure of PF4a is shown on the left. **c**, Cryo-EM density of the PF4a binding site observed in NaCT. The inhibitor binds in an orientation similar to that of Rotamer-1 in NaDC3. The densities for the protein and the inhibitor are contoured at 6σ.

nature portfolio

Corresponding author(s): Wang DN, Mindell JA

Last updated by author(s): Jul 29, 2024

Reporting Summary

Nature Portfolio wishes to improve the reproducibility of the work that we publish. This form provides structure for consistency and transparency in reporting. For further information on Nature Portfolio policies, see our Editorial Policies and the Editorial Policy Checklist.

Statistics

For all statistical analyses, confirm that the following items are present in the figure legend, table legend, main text, or Methods section.

n/a	Confirmed
☐	☒ The exact sample size (*n*) for each experimental group/condition, given as a discrete number and unit of measurement
☐	☒ A statement on whether measurements were taken from distinct samples or whether the same sample was measured repeatedly
☐	☒ The statistical test(s) used AND whether they are one- or two-sided *Only common tests should be described solely by name; describe more complex techniques in the Methods section.*
☒	☐ A description of all covariates tested
☒	☐ A description of any assumptions or corrections, such as tests of normality and adjustment for multiple comparisons
☐	☒ A full description of the statistical parameters including central tendency (e.g. means) or other basic estimates (e.g. regression coefficient) AND variation (e.g. standard deviation) or associated estimates of uncertainty (e.g. confidence intervals)
☐	☒ For null hypothesis testing, the test statistic (e.g. *F*, *t*, *r*) with confidence intervals, effect sizes, degrees of freedom and *P* value noted *Give P values as exact values whenever suitable.*
☒	☐ For Bayesian analysis, information on the choice of priors and Markov chain Monte Carlo settings
☒	☐ For hierarchical and complex designs, identification of the appropriate level for tests and full reporting of outcomes
☒	☐ Estimates of effect sizes (e.g. Cohen's *d*, Pearson's *r*), indicating how they were calculated

Our web collection on statistics for biologists contains articles on many of the points above.

Software and code

Policy information about availability of computer code

Data collection	Leginon (v 3.5) and Leginon (v 3.6)
Data analysis	Cryo-EM micrographs were processed using CryoSparc (v 3.3.1 and v 4.4.1), MotionCor2 (v 1.5), CTFFIND4 (v 4.1.13), Relion-4.0, WARP (v 1.0.9), Topaz. Maps and models were analyzed using Phenix (v 1.19), Coot (v 0.9.6), ChimeraX-1.4, Chimera (v 1.15), PyMOL (v 2.5.2), ISOLDE, Chemical Sketch. Substrate binding data measuring by fluorescence quenching were analyzed using GraphPad Prism (v 10.2.3). Transport activity was analyzed using GraphPad Prism (v 9.4.1). Voltage-clamp was processed using pClamp 10. NMR spectra were analyzed using Topspin (v 4.1.1).

For manuscripts utilizing custom algorithms or software that are central to the research but not yet described in published literature, software must be made available to editors and reviewers. We strongly encourage code deposition in a community repository (e.g. GitHub). See the Nature Portfolio guidelines for submitting code & software for further information.

Data

Policy information about availability of data

All manuscripts must include a data availability statement. This statement should provide the following information, where applicable:

- Accession codes, unique identifiers, or web links for publicly available datasets
- A description of any restrictions on data availability
- For clinical datasets or third party data, please ensure that the statement adheres to our policy

The cryo-EM densities and protein models have been deposited to the Electron Microscopy Data Bank and Protein Data Bank for the NaDC3-Succ-Coo-Coo (EMD-42621, PDB: 8UVI), NaDC3-Succ-Coo-Ci (EMD-42617, PDB: 8UVE), NaDC3-DMS-Co-Ci (EMD-42619, PDB: 8UVG), NaDC3-DMS-Ci-Ci (EMD-42618, PDB: 8UVF), NaDC3-aKG-Ci-Ci (EMD-42615, PDB: 8UVC), NaDC3-PF4a-Ci-Ci (EMD-42616, PDB: 8UVD), NaCT-Succ-Ci-Ci (EMD-42620, PDB: 8UVH) and NaCT-PF4a-Ci-Ci (EMD-42614, PDB: 8UVB) complexes. Source data for functional studies of the transporter have been uploaded to the journal's website.

Research involving human participants, their data, or biological material

Policy information about studies with human participants or human data. See also policy information about sex, gender (identity/presentation), and sexual orientation and race, ethnicity and racism.

Reporting on sex and gender	N/A
Reporting on race, ethnicity, or other socially relevant groupings	N/A
Population characteristics	N/A
Recruitment	N/A
Ethics oversight	N/A

Note that full information on the approval of the study protocol must also be provided in the manuscript.

Field-specific reporting

Please select the one below that is the best fit for your research. If you are not sure, read the appropriate sections before making your selection.

☒ Life sciences ☐ Behavioural & social sciences ☐ Ecological, evolutionary & environmental sciences

For a reference copy of the document with all sections, see nature.com/documents/nr-reporting-summary-flat.pdf

Life sciences study design

All studies must disclose on these points even when the disclosure is negative.

Sample size	The transport and inhibition study sample sizes of N=3 for each time and concentration point were chosen to ensure reproducibility based on prior experimental experience (https://doi.org/10.1038/s41586-021-03230-x). The substrates as succinate, α-ketoglutarate, 2,3-DMS binding study sample size of N=3-4 was chosen for the same reason.
Data exclusions	No data were excluded from the analysis.
Replication	Inhibition assay of each mutant was performed using three technical replicates in each of three separate transfections on separate days (biological replicates). Transport assays were preformed using three technical replicates in each of three biological replicates. Three independent inhibition biological experiments and three independent transport assays were applied in total and all replicates were successful. For the kinetics of succinate uptake, two technical replicates in each of two biological replicates were measured and all replicates were successful. The substrate binding assays of succinate and α-ketoglutarate were measured in triplicate in each of three separate experiments on separate days. The substrate binding assays of 2,3-DMS were measured in triplicate in each of four separate experiments on separate days. Three and four independent biological experiments were applied in total and all replicates were successful.
Randomization	For cryo-EM studies, particles were randomly assigned to half-maps for resolution determination. No randomization was used for transport, inhibition or substrate binding assays.
Blinding	Blinding was not used for structural or transport experiments. The results are not subjective or prone to being biased by individual investigators, therefore blinding is not necessary.

Reporting for specific materials, systems and methods

We require information from authors about some types of materials, experimental systems and methods used in many studies. Here, indicate whether each material, system or method listed is relevant to your study. If you are not sure if a list item applies to your research, read the appropriate section before selecting a response.

Materials & experimental systems

n/a	Involved in the study
☒	☐ Antibodies
☐	☒ Eukaryotic cell lines
☒	☐ Palaeontology and archaeology
☒	☐ Animals and other organisms
☒	☐ Clinical data
☒	☐ Dual use research of concern
☒	☐ Plants

Methods

n/a	Involved in the study
☒	☐ ChIP-seq
☒	☐ Flow cytometry
☒	☐ MRI-based neuroimaging

Eukaryotic cell lines

Policy information about cell lines and Sex and Gender in Research

Cell line source(s)	ATCC (HEK293), EcoCyte (Xenopus laevis Oocytes), Expression systems (Tni and SF9).
Authentication	Cell lines were not authenticated.
Mycoplasma contamination	Not performed
Commonly misidentified lines (See ICLAC register)	Cell lines used are not among the commonly misidentified lines.

Plants

Seed stocks	N/A
Novel plant genotypes	N/A
Authentication	N/A